6-1-1992

Design and fabrication of an air-bridge microphone

Paul L. Jeran

Design and Fabrication of an Air–Bridge Microphone

by
Paul L Jeran

A Thesis Submitted in Partial Fulfillment
of the Requirements for the Degree
of
MASTER OF SCIENCE
in
Mechanical Engineering

Approved by:

Mark H. Kempski, Ph.D.
Rochester Institute of Technology (Thesis Advisor)

Joseph S. Torok, Ph.D.
Rochester Institute of Technology

Lynn F. Fuller, Ph.D.
Rochester Institute of Technology (Department Head, Microelectronic Engineering)

Charles W. Haines, Ph.D.
Rochester Institute of Technology (Department Head, Mechanical Engineering)

Department of Mechanical Engineering
College of Engineering
Rochester Institute of Technology
Rochester, New York 14623

June 1992

Title of Thesis

Design and Fabrication of an Air–Bridge Microphone

I, Paul L Jeran, grant permission to the Wallace Memorial Library to reproduce my thesis in whole or in part. Any reproduction will not be for commercial use or profit.

The author makes no claims as to the reliability of the methods, procedures, or results within the enclosed report for the purposes of medical diagnosis, treatment, or prognosis.

7/15/92

Date

Abstract

Today's hearing aids have many shortcomings: they are susceptible to environmental damage, cannot be worn while sleeping or in wet environments, are obtrusive and are expensive. New technologies are being developed which allow most all of these shortcomings to be addressed by placing a portion of the hearing aid within the middle ear. These new technologies require size reductions in several of the aid components, one of these being the microphone. Microelectromechanical Systems (MEMS) has already developed technologies that can be used to construct these microphones. Most microphones constructed using MEMS techniques employ a dual wafer design, the microphone membrane is constructed on one wafer and attached to a second wafer containing bonding pads and possibly additional sensing elements. The use of two wafers to manufacture one microphone reduces the yield of the process and requires an additional alignment and bonding step. Further, the methods used for fabrication are non-traditional and do not allow appropriate electronics to be easily fabricated with the microphone.

An alternative approach is being investigated by this thesis. Here a single wafer and standard microelectronic processing techniques are used to fabricate the diaphragm, sensing elements and bonding pads. This approach will simplify construction and allow the possibility of including appropriate signal processing electronics on the microphone die. Equations are developed to predict the static and dynamic deflection and natural frequency of the microphone system. Optimal design strategies are used to minimize the microphone diaphragm area subject to electrical and mechanical constraints. A first generation microphone was fabricated. However, unanticipated processing constraints on the microphone design rendered the microphones inoperable. Several design modifications are noted to solve these problems and promote the successful fabrication of second generation microphones.

Acknowledgements

A multidisciplinary effort such as this requires the dedication and perseverance of several people in order to succeed. I have been fortunate enough to have had such people working with me on this project. Dr. Mark Kempski was willing to allow me to pursue an unorthodox thesis topic and give me guidance and encouragement along the way. Dr. Lynn Fuller gave me, a student outside of his department, access to the cleanroom and processing facilities, as well as educating me in microelectronic fabrication techniques. Dr. Joseph Török and Dr. Hany Ghoneim took the time to answer my questions on mechanics and vibrations, no matter how trivial. I would like to thank Jim Ramier, Todd Kortekamp and and Renée Jessome for keeping me sane and putting up with my ranting and raving. Finally I would like to thank my family for the support and encouragement that was always offered, along with the the occasional shove to get me going again. I will never forget the efforts of several others, too countless to mention, but I must give a large word of thanks to the secretaries of both the Mechanical and Microelectronic departments, as well as the staff of the machine shop and cleanroom. In conclusion, I thank you all for what you have done, but more importantly what you have shown me I could do for myself, for these are the things that I will carry with me for the rest of my life.

Paul L Jeran
Yarmouth, N.S.

Contents

List of Figures

1 Introduction

In the United States one of every 1000 children is born with a hearing disability. Thirty percent of elderly Americans suffer from some level of hearing impairment. This equates to between 16-21.5 million persons that suffer some level of hearing impairment in the United States[1]. A large group of this population uses some form of hearing assistance.

Hearing assistance can take many forms. Persons with minor volume attenuation may employ a simple telephone handset amplifier to communicate with the outside world. For others complex surgical procedures are required to provide even a small degree of auditory awareness. Between these two extremes there are approximately four million people that depend on a full time insertable hearing aid[1].

In the past decade many advances have been made in hearing aid technology. Behind-The-Ear (BTE; Figure 1) hearing aids have become smaller and more programmable to meet each individual's needs.

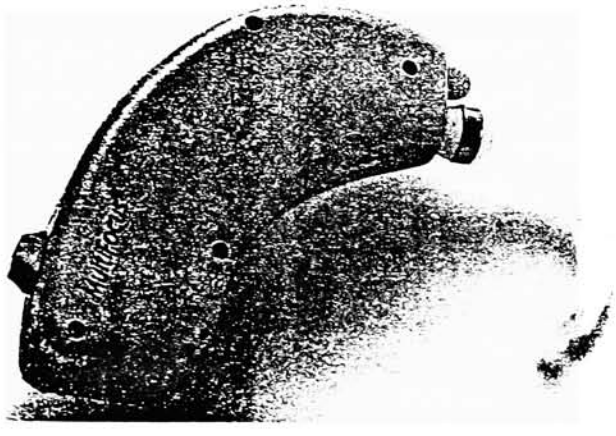

Figure 1: Behind the Ear Hearing Aid (BTE)

In-The-Ear (ITE; Figure 2) hearing aids have been developed that provide the same features of the BTE hearing aids in a smaller and less obtrusive package.

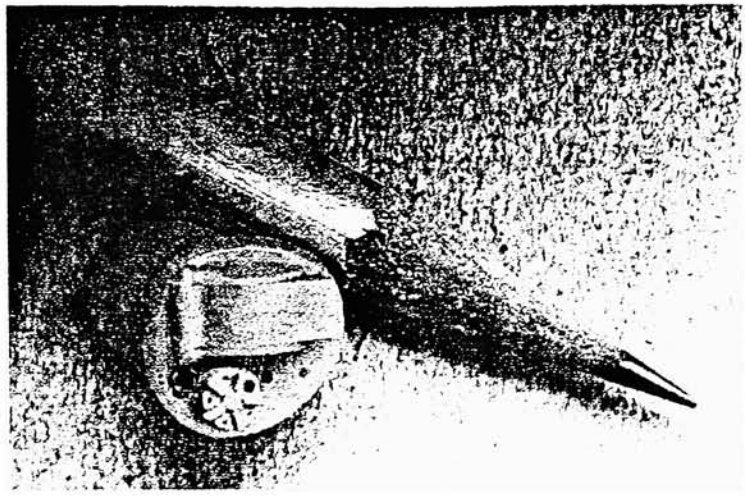

Figure 2: In The Ear Hearing Aid (ITE)

Finally, cochlear implants (Figure 3) are being developed that provide auditory assistance to people that do not benefit from amplification-type aids via direct nerve stimulation.

Each of these devices has its advantages and disadvantages. Most people prefer the smaller ITE type hearing aid to the BTE aid for cosmetic reasons, but the ITE aid is more expensive. Both external aids are susceptible to environmental damage such as water and dirt contamination. Coupling distortion is also prevalent due to the air column which is trapped between the earmold and eardrum. In addition, certain individuals cannot wear external hearing aids due to ear drainage problems. Cochlear implants require external units to be carried to provide power and signal processing to the internal implant. All three types of aids are usually removed for sleep, reducing the users awareness to auditory warning while asleep (ie., firealarm, baby crying, burglar). Technological advances have lessened the severity of many of the aforementioned problems, by reducing the size or increasing the sturdiness of the aids, but the problems still exist albeit to a lesser extent.

One of the major hurdles facing a hearing impaired individual is psychological. Even though a hearing aid may provide a better awareness to the auditory world,

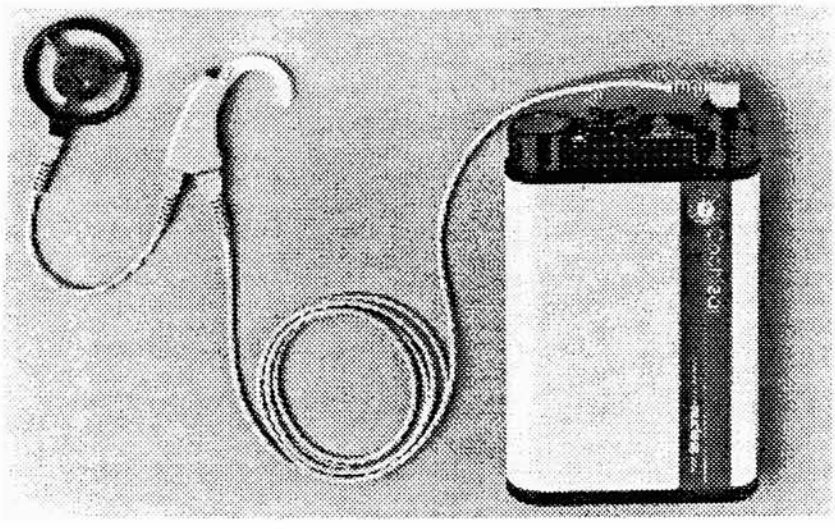

Figure 3: Cochlear Implant

many users refuse to wear an aid because it identifies them as an individual with a disability[8]. The device that provides them with equality in the hearing world also marks them as a person that is physically challenged. It is for this reason that ITE aids are more popular, but even these aids are visible.

A hearing aid is therefore warranted which is unobtrusive while allowing the physiologic, cosmetic and psychologic needs of the user to be satisfied. It should be impervious to elemental damage, allow the user an unrestricted lifestyle, and function continuously so that the wearer can respond to audio warnings while asleep or in the shower. Finally, the "ideal" hearing assist device should be available at an affordable price.

Work on such "ideal" hearing aids have been documented[8]. Partially implantable hearing aids have been developed (Figure 4) that are less obtrusive than current aids, but they still have external battery, microphone, and signal processing circuitry. These devices are, however, costly.

If the size of the microphone and electronics could be reduced to a small enough package, then the entire aid, minus a power source, could be placed in the ear canal or even the middle ear. This miniaturization would solve several problems. The

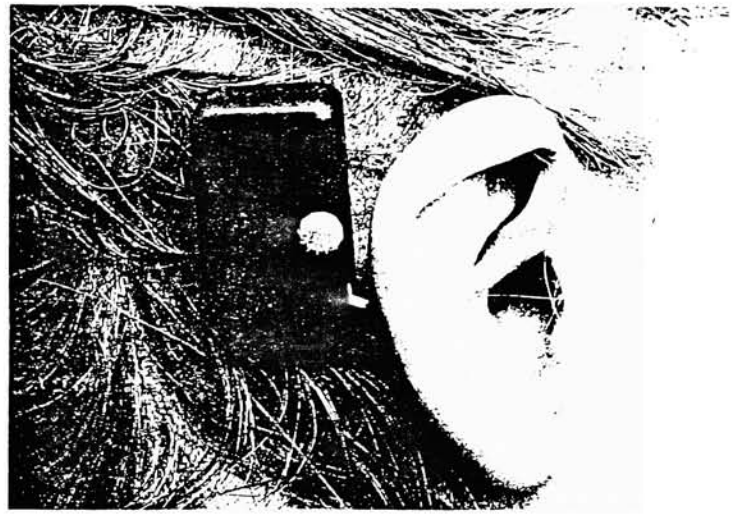

Figure 4: Partially Implanted Hearing Aid

electronics would be protected from the elements. The wearer would receive audio cues from the ear region giving a better perception of sound direction. No air-column effects would have to be considered when transmitting sound into the ear. Finally, the hearing aid could feasibly be left active at all times allowing the user to take action on auditory cues at anytime.

The goal of this research thesis is to design and construct a first generation implantable hearing aid system. To this end, a microphone will be designed that can be fabricated using microelectronic construction techniques such that all signal processing electronics could be incorporated on the same chip. Post-fabrication acoustic testing protocols to 'benchmark' microphone performance will likewise be detailed.

2 Background

2.1 History

2.1.1 Construction Techniques

The field of Micro-ElectroMechanical Systems (MEMS) has experienced tremendous growth in the past few years. This growth has been driven by the potential to produce quality, low cost sensors in bulk with integrated signal processing capabilities. The technologies that have allowed MEMS to emerge and grow to what it is today were developed in the late 1960's by researchers at Bell Telephone Laboratories[17].

This early work developed beam-lead air isolated Integrated Circuits (IC) which allow one trace on a IC to pass over another with only air separating the two contacts. The fabrication methods developed to achieve this were anisotropic etch processes where deep pits could be etched in the the silicon surface by selectively etching certain silicon crystal planes.

Further developments during the 1970's made anisotropic etch technologies commercially viable[17]. Anisotropic etch processes have been further combined with surface mask techniques (i.e., using SiO_2, Si_xN_y, heavily doped silicon) to provide several types of beam or diaphragm structures (Figure 5).

For most of these devices, the final processing step would be the anisotropic etch. The etch step could take several hours, depending on the thickness of the starting silicon wafer, and the geometry desired. This processing technique is known as bulk machining, due to the removal of the bulk of the silicon. The anisotropic etch usually forms the mechanical element of the device (i.e., membrane or cantilever). After the final etch, a micromachined sensing element is typically bonded to another silicon wafer or a glass plate to complete the sensor assembly. Such bonded wafer designs are currently being used in the automotive industry as mass flow sensors. Figure 6 shows a thermopile gas flow sensor. The cantilevered beam holds a polysilicon heating element and two thermocouples.

Early bulk machined designs still had the problem that two wafers had to be bonded together to form the final sensor. Bonding has the effect of lowering the yield

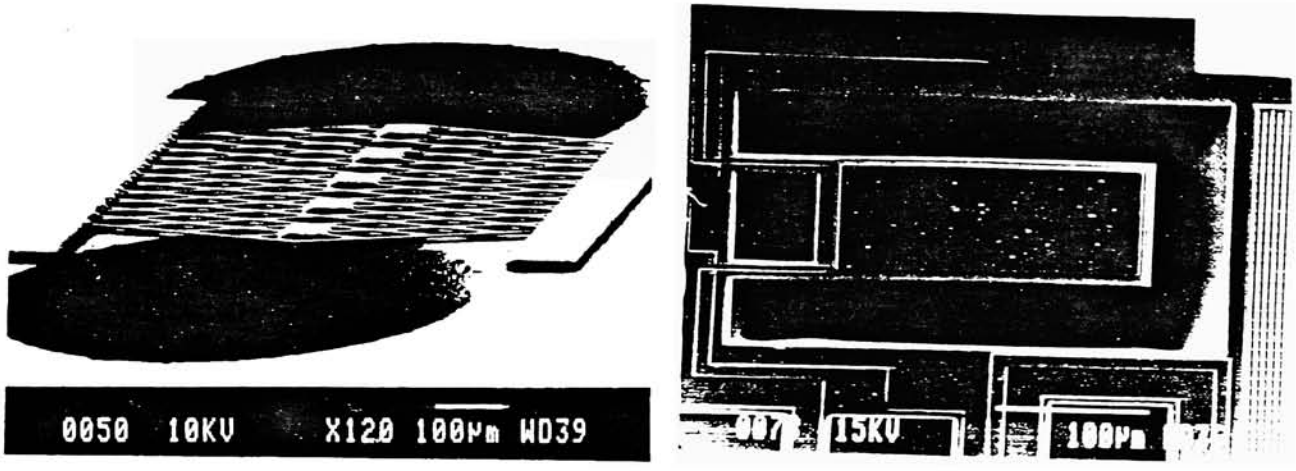

Figure 5: Bulk Micromachined Devices

of the process due to misalignment and poor adhesion of the wafers. Alternative processing techniques have been developed[17] based on the aforementioned work in air isolated IC's and electrostatically driven microstructures[17]. Here, a "sacrificial layer" is used to elevate a plate or sandwich of plates off of the silicon surface. After deposition of the top material(s), the sacrificial layer is selectively etched away, freeing the top structure from the silicon surface. Figure 7 shows two examples of devices fabricated using this technique. In the left picture, an impact hammer and test target have been constructed. The impact hammer is driven by an electrostatic comb drive. and the target is mounted on a spring. The picture on the right shows a geartrain. The sacrificial layer technique is used for microphone construction in the current study.

2.1.2 Microphone Design

After constructing a pressure transducer using microfabrication techniques, a logical next step would be to tune the transducer to provide a uniform response in the audio range of frequencies and pressures. Such an approach was first employed in 1983 by Royer, et al.[14], where a microphone was constructed by bulk machining a silicon

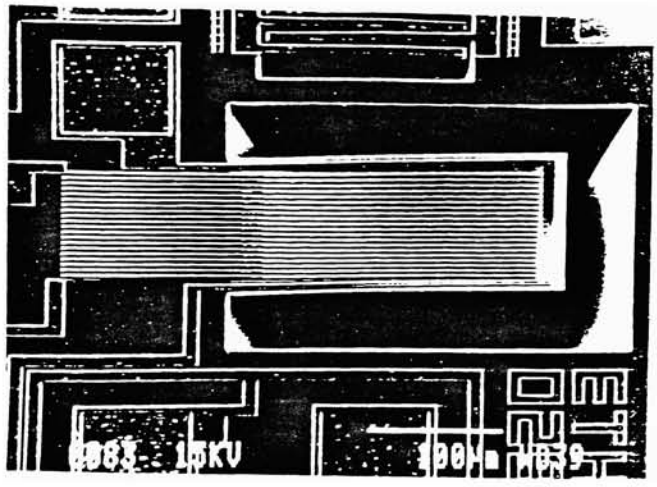

Figure 6: Automotive Mass Flow Sensor

wafer to produce a 30μm thick, 3mm diameter diaphragm. On one side of this diaphragm, a 3μm layer of ZnO film was sandwiched between two electrodes. When the diaphragm deflected, the ZnO sandwich would also deflect, producing a piezoelectric signal. This signal was then amplified by a high impedance MOS (Metal Oxide Semiconductor) amplifier (Figure 8). Although the the response of the microphone was not up to the quality of commercially available microphones, it did prove the viability of using micromachining to produce audio sensors.

Further improvements in microfabrication and new methods of sensing membrane deflection have produced smaller microphones with better response characteristics than the original ZnO microphone[14]. A brief listing of the microphones made using MEMS technology is in Table 1.

One of the first microphones to use a capacitance change as the output signal was developed in 1985 by Kühnel, et al.[14, 10] The microphone had a two wafer design, and used bulk machining process to form the diaphragm and back plate. The diaphragm was a laminate of aluminium and silicon nitride, 100nm and 150nm thick, respectively. The diaphragm dimensions were 800μm x 800μm with a plate separation of 2μm. (Figure 9) This microphone had better response characteristics than the ZnO

Author,year	Transducer Principal	Membrane material. size (mm^2)	Resonance frequency (kHz)	Sensitivity (mV/Pa)	Capacitance or impedance
Royer, 1983	piezoelectric (3 μm ZnO)	30μm Si 3 x 3	~40	0.25	
Holm, 1985	condenser (28 V bias)	0.15μm Si_xN_y 0.8 x 0.8	>20	4.3	1.4pF
Muller, 1987	piezoelectric (3 μm ZnO)	2μm Si_xN_y 3 x 3	7.8	0.05	26pF
Franz,1988	piezoelectric (0.2μm AlN)	0.8μm doped Si 0.8 x 0.9	45	0.025	75pF
Bergqvisit. 1990	condenser (16 V bias)	5μm doped Si 2 x 2	4	13	3.5pF
Kühnel, 1990	FET	0.15μm doped Si 0.7 x 1.3	>20	0.6 (at 1kΩ)	1kΩ
Kühnel, 1991	condenser (28 V bias)	0.15μm Si_xN_y 0.8 x 0.8	>20	7.3	1.1pF

Table 1: Previously constructed MEMS based microphones

Figure 7: Surface Micromachined Devices

microphone, but still less than that of contemporary commercial microphones.

One of the major factors contributing to the poor response of dual wafer microphones is that the thin air-gap between the microphone plates introduces a large air damping factor, which affects high frequency response. A solution to this problem was to add grooves to the bottom plate (Figure 10)[14]. The grooves directed the air to holes in the bottom wafer with low resistance to flow, thereby decreasing the air damping. Microphones with commercial-quality frequency response have been constructed using this configuration[14].

Another method of reducing the air-gap damping is to reduce the lower plate dimensions relative to the air gap dimension. Such an approach uses the change in capacitance to change the characteristics of a Field Effect Transistor (FET) as opposed to the signal itself. Using this sensing technique, the dimensions of the lower plate could be decreased to 110μm for the same 800μm x 800μm top plate, significantly decreasing air-gap damping. The same membrane design of Kühnel[10] was employed to construct a microphone with a two wafer design(Figure 11)[12]. The lower wafer contains the source and drain regions along with a P-doped channel. The upper wafer contains an Al-Si_xN_y membrane acting as the gate. Using this

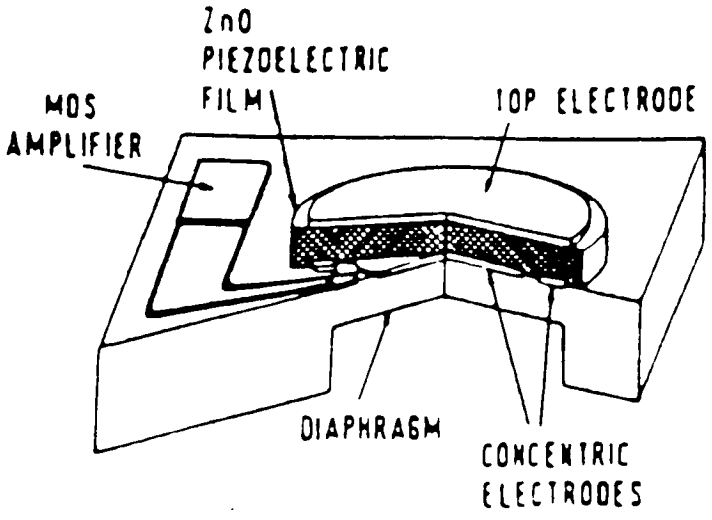

Figure 8: First Micromachined Microphone

sensing arrangement, response characteristics were obtained which were comparable to commercial microphones[12].

For the present investigation of air–bridge microphones, a plate capacitor sensing arrangement has been used.

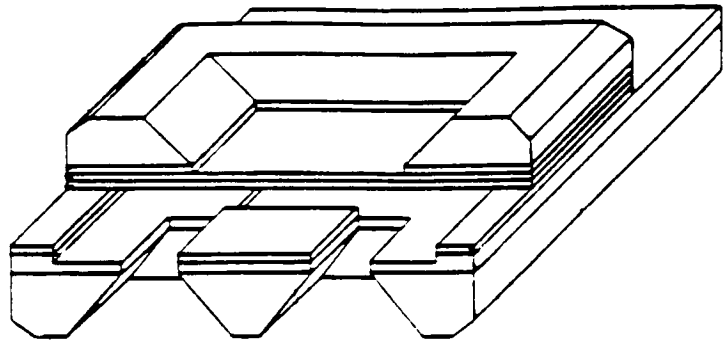

Figure 9: First Capacitive Microphone, University of Darmstadt, 1985

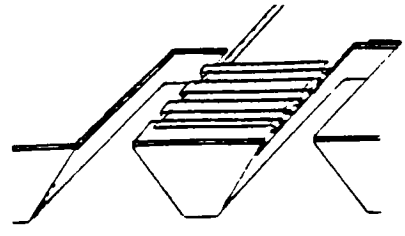

Figure 10: Grooving on the back plate to reduce air damping

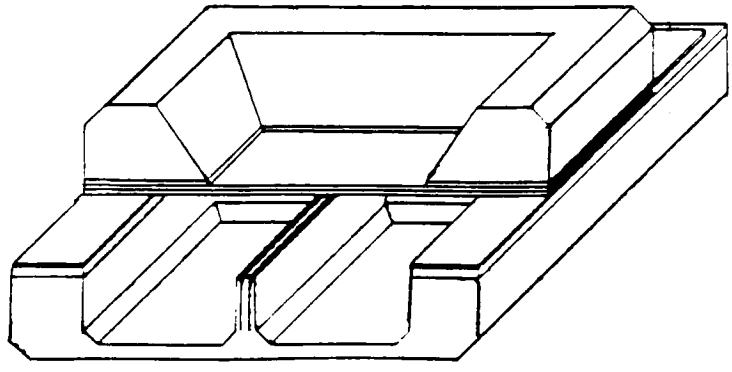

Figure 11: A FET Sensing Microphone

2.2 The Ear

Before a microphone can be designed to augment the sensing organs of the ear, it is necessary that we understand how sound is sensed in humans.

2.2.1 Physiology

As a sound wave travels through the air and into the ear, it encounters the outer, middle and inner stages (Figure 12). The outer ear consists of three major parts; the pinna, meatus and tympanic membrane (eardrum).

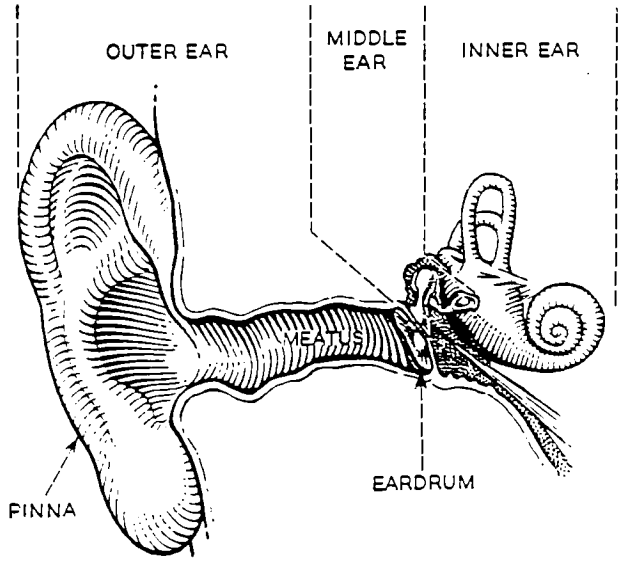

Figure 12: The Ear

The pinna does some directing of sound into the meatus, but does not play much of a role in the hearing process. The second part, the meatus (Figure 12), acts as an amplifier of sound. Due to its closed end tube-like structure it acts similar to a pipe organ tube and is tuned to frequencies between 2000–5500Hz. In this frequency range, the sound pressure level (SPL) at the tympanic membrane differs from the SPL at the pinna by +5dB to +10dB.

In the middle ear as the sound waves impinge upon the eardrum, the sonic energy is converted into mechanical motion. In normal conversational situations (≈60dB) the deflection of the eardrum is on the order of $1x10^{-10}$m (1 Å). This motion is then

transferred through the middle ear by three bones: the malleus, incus and stapes (hammer, anvil and stirrup) as depicted in Figure 13.

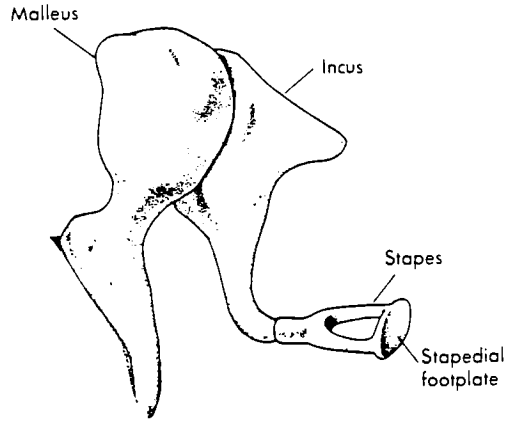

Figure 13: The Malleus, Incus and Stapes (Ossicles)

These bones act as an amplification and impedance matching system between the outside world and the inner ear. The linkage formed by these three bones reduces the motion at the eardrum to motion at the oval window (entrance to the inner ear) by 1.3-3 times. This reduction in motion equates to a proportional increase in force. Another amplification mechanism acting in the middle ear is a piston arrangement. The area of the eardrum is 15-30 times larger than that of the oval window. This acoustic piston increases the force on the oval window due to the mismatch in surface area over which sound pressure is applied. The main reason for both of these amplification mechanisms is to allow the transfer of energy from the less dense and compressible air of the outside world to the dense, incompressible fluid-filled inner ear. Another function of the middle ear is that of a check valve for loud noises. In a feedback loop similar to that of the iris in the eye, the muscles holding the ossicles in contact with each other and the eardrum pull the bones apart to change the motion of the linkage, decreasing the amplification. Another set of muscles contract and increase the rigidity of the eardrum, decreasing the amplitude of its vibration.

As the stapes presses upon the oval window, the once sonic input is transferred to the inner ear. The inner ear converts physical motion to an electrical signal which is transferred via the eighth cranial nerve to the brain. The main element in the inner ear is the cochlea. It is inside this fluid-filled spiral shaped organ that the nerves interface with the rest of the ear. If the cochlea were unrolled it would appear as depicted in Figure 14.

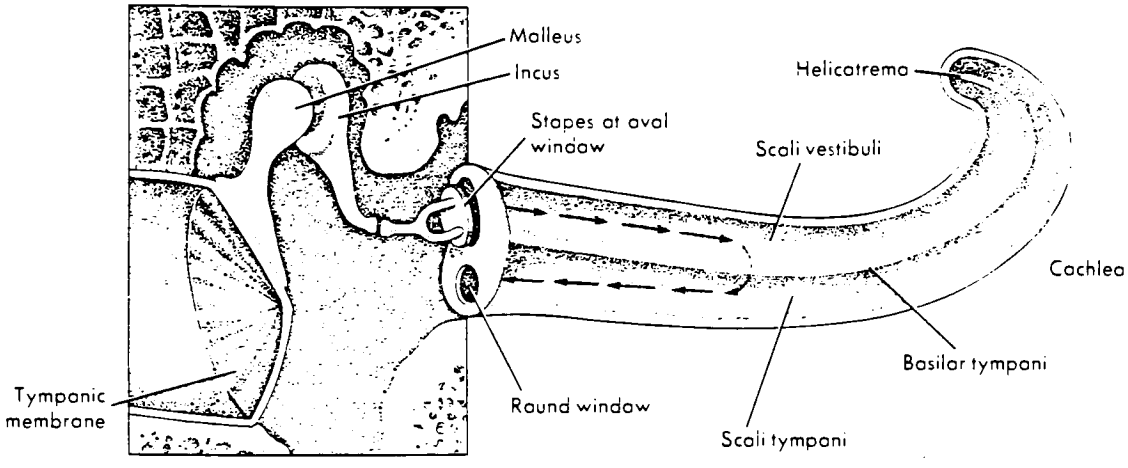

Figure 14: The Cochlea

The membrane envelope in the middle contains the sensing organs of the cochlea (Organ of the Corti), and the connections to the nervous system(Figure 15). As a wave of certain frequency travels through the cochlea a section of the center membrane is set in vibration with a localized standing wave. The peak amplitude of this wave occurs in the area of the membrane tuned to that frequency. The center membrane is composed of two other membranes (Reissner's and Basilar) that sandwich the actual sensing elements of the cochlea.

This wave causes both bending and shearing forces to be exerted on the hairs which in turn produce electrical signals that are carried to the brain. The exact electrical interactions of the inner ear are not yet fully understood. Even for a pure tone signal, the hairs around the excited area of the center membrane are not the only ones to

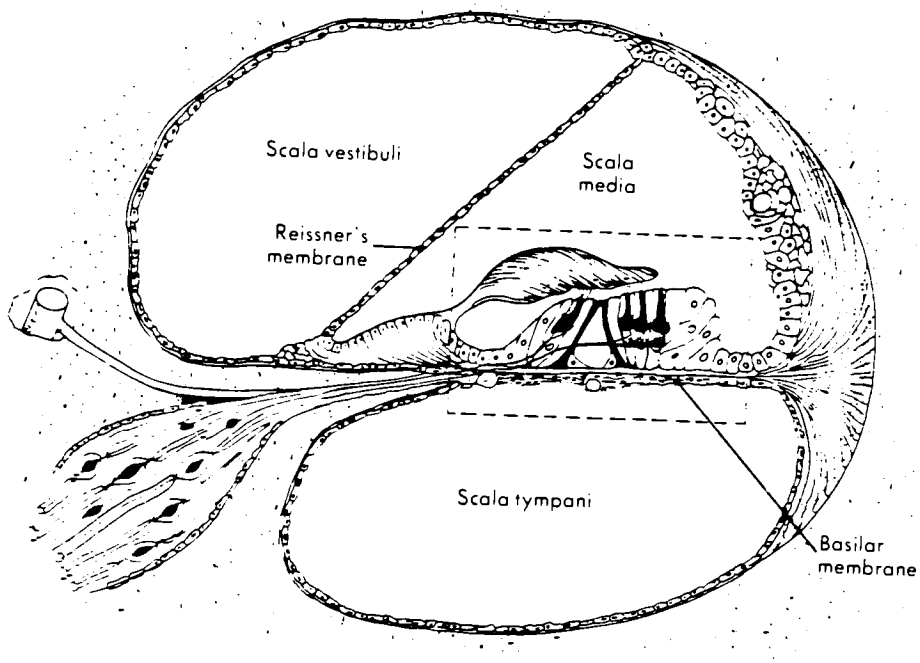

Figure 15: The Hair Cells, Organ of the Corti

contribute to the electrical signal. These electrical signals are then transmitted to the brain where the signals from the left and right ear are processed to give directionality and selectivity.

2.2.2 Capabilities

The ear is quite a versatile instrument. It is sensitive to frequencies that range from 20-20,000Hz. In this frequency range the ear can sense sound pressure levels (SPL) from 20μPa (0dB, threshold of hearing) to 200Pa (140dB, threshold of pain). The ear can differentiate between two signals differing by as little as 100μPa (3dB). It is not equally sensitive to all frequencies. A graph of the sensitivity of the ear with varying frequency is shown in Figure 16.

The lines in Figure 16 are curves of constant perceived intensity. For example, a 50Hz tone must be 85dB to sound as loud as 1000Hz tone at 70dB. It can be seen from this graph that the ear is most sensitive in the 2000-5000Hz range. Part of this is due to the amplification caused by the meatus.

The ear has a response time of about 70ms. Sounds shorter than this time are referred to impulses, and are not perceived as being as loud as a sound at the same

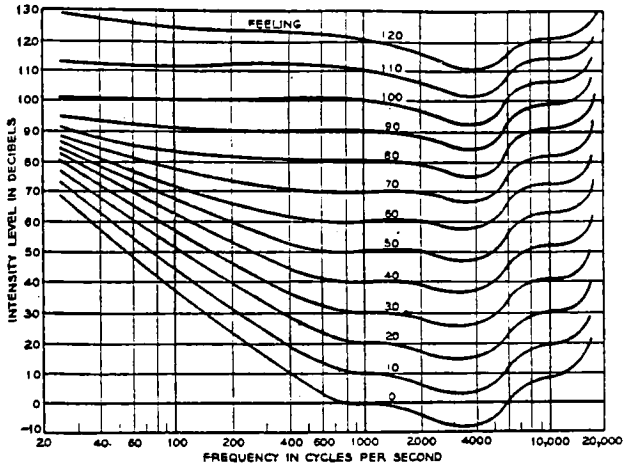

Figure 16: Lines of constant perceived loudness

intensity, but sensed for a longer period of time. Sound impulses are dangerous because they damage the ear, but are not sensed as being painfully loud.

2.2.3 Impairment Types

There are several ways that the ear can be damaged: exposure to loud noises, illness, and birth defects.

Exposure to repeated loud noises is probably the principal cause of hearing impairment. We are all exposed to short duration loud noises in everyday life. A power drill or saw, fire alarms, and planes taking off are all examples of loud noises that have the capability of causing a temporary or permanent hearing loss to occur. When a loud noise enters the ear, the magnitude of the force causes the hair cells in the organ of the corti to be flattened out. After repeated assaults on the ear, these cells die, and the supporting cells become enflamed. Further assaults will cause these cells to die, and eventually the organ of the corti can collapse. This damage also occurs as part of the aging process.

Several illnesses can cause hearing impairment. Some of the more common illnesses to induce hearing impairment are Rubella, Measles, Mumps and Otitis Media

(middle ear infection). The first three of these illnesses attack the eighth cranial nerve. These can be prevented by proper vaccination. Otitis Media causes build up of fluid in the middle ear to the point that the tympanic membrane ruptures. The scar tissue formed on the tympanic membrane results in a decreased sensitivity causing attenuated hearing. Adverse drug interaction/dosage can also induce temporary and permanent hearing loss.

Finally, hearing impairment can be caused by birth defects. These can range anywhere from deformation of the pinna to complete absence of one or all of the components of the ear.

3 Theory

To design the microphone, at least five parameters must be calculated. These are the static and dynamic deflections of the beam, the microphone capacitances at these deflections, and the first resonant frequency of the microphone. Plate theory was initially investigated for modeling the mechanical parameters of the microphone. Later it was found that due to manufacturing constraints, the microphone membrane would be long and thin, making beam theory more applicable to the problem.

3.1 Static Deflection

The static deflection of the microphone can be modeled using a beam of length, L, and cross-section, a, clamped at both ends. A uniform pressure load, w, is applied to the top surface (Figure 17).

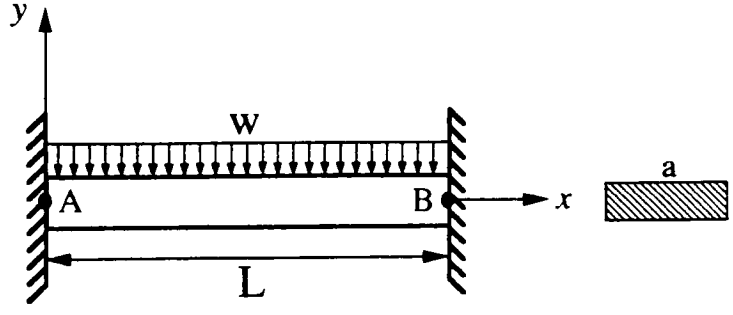

Figure 17: Model for static deflection

Drawing the free body diagram (Figure 18), we can write the equations of equilibrium:

$$\Sigma F_x = 0 \;:\; A_x - B_x = 0 \tag{1}$$

$$\Sigma F_y = 0 \;:\; A_y + B_y - wL = 0 \tag{2}$$

$$\Sigma M_A = 0 \;:\; M_A + LB_y - \frac{1}{2}wL^2 - M_B \tag{3}$$

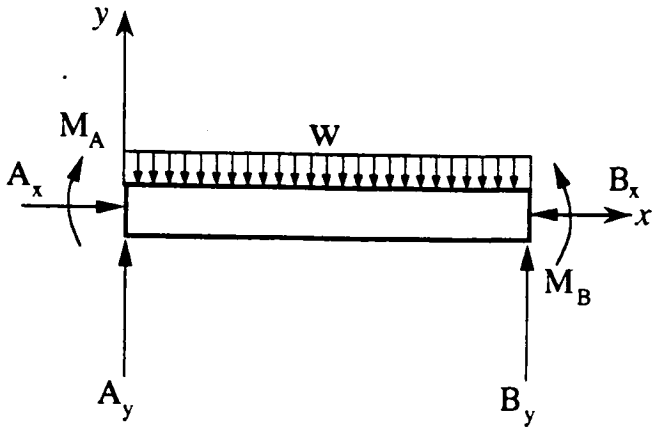

Figure 18: Free body diagram for static analysis

Equation 1 describes the equilibrium of the beam in the axial direction, while Equations 2 and 3 reflect the transverse and planar moment equilibrium, respectively. Euler–Bernoulli beam theory is assumed. Inherent symmetries in geometry, loading, and material properties dictate that $A_x = B_x = 0$. Looking at the remaining equations, it is noted that there are four unknowns (A_y,B_y,M_A,M_B) and only two relevant equations. Again symmetry considerations may be invoked to yield $A_y = B_y$ and $M_A = M_B$, where substitution into equations 2 and 3 allows each reaction to be determined. An alternative approach, which also solves for the lateral deflection of the beam, is described below.

Sectioning the beam at some arbitrary point, C, drawing the accompanying free body diagram (Figure 19), and summing moments about C allows the deformed shape to be determined.

$$\Sigma M_C = 0 : \; M + \frac{1}{2}wx^2 + M_a - A_y x = 0 \tag{4}$$

Noting that the governing equation for the deflection of an Euler beam is:

$$\frac{d^2y}{dx^2} = \frac{M(x)}{EI} \tag{5}$$

Hence, upon substitution of equation 4 into 5 we can write

$$\frac{d^2y}{dx^2}EI = A_y x - M_A - \frac{1}{2}wx^2 \tag{6}$$

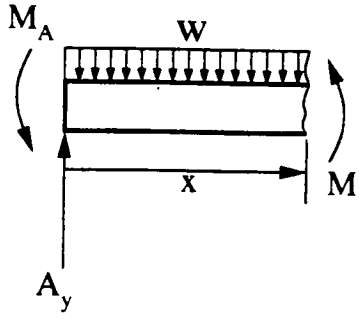

Figure 19: Sectioning of beam to sum moments

Integrating with respect to x we obtain

$$\frac{dy}{dx}EI = \frac{1}{2}A_y x^2 - M_A x - \frac{1}{6}wx^3 + C_1. \tag{7}$$

Noting that $\frac{dy}{dx} = \tan\theta \approx \theta$ for small angles allows equation 7 to be rewritten as:

$$EI\theta = \frac{1}{2}A_y x^2 - M_A x - \frac{1}{6}wx^3 + C_1 \tag{8}$$

Integrating equation 7 with respect to x yields the deflection equation of the beam

$$EIy = \frac{1}{6}A_y x^3 - \frac{1}{2}M_A x^2 - \frac{1}{24}wx^4 + C_1 x + C_2. \tag{9}$$

Using the boundary conditions to solve for the constants C_1 and C_2:

$$\begin{aligned} y(0) = 0 \quad &\Rightarrow \quad C_2 = 0 \\ \tfrac{dy}{dx}(0) = \theta(0) = 0 \quad &\Rightarrow \quad C_1 = 0 \end{aligned}$$

and substituting back into equation 9:

$$EIy = \frac{1}{6}A_y x^3 - \frac{1}{2}M_A x^2 - \frac{1}{24}wx^4. \tag{10}$$

Applying the boundary conditions from the other side of the beam yields two more equations:

$$y(L) = 0 \Rightarrow -\frac{1}{24}wL^4 + \frac{1}{6}A_yL^3 - \frac{1}{2}M_AL^2 = 0 \quad (11)$$

$$\theta(L) = 0 \Rightarrow -\frac{1}{6}wL^3 + \frac{1}{2}A_yL^2 - M_AL = 0 \quad (12)$$

Rewriting equations 2, 3, 11, 12:

$$\begin{array}{ccccccccc} A_y & + & B_y & + & 0 & + & 0 & = & wL \\ 0 & + & LB_y & + & M_A & - & M_B & = & \frac{1}{2}wL^2 \\ \frac{1}{6}L^3A_y & + & 0 & - & \frac{1}{2}L^2M_A & + & 0 & = & \frac{1}{24}wL^4 \\ \frac{1}{2}L^2A_y & + & 0 & - & LM_A & + & 0 & = & \frac{1}{6}wL^3 \end{array}$$

Solving for A_y, B_y, M_A, M_B yields:

$$A_y = \frac{1}{2}wL \; ; \; B_y = \frac{1}{2}wL \; ; \; M_A = \frac{1}{12}wL^2 \; ; \; M_B = \frac{1}{12}wL^2.$$

Where the shape curve (equation 10) can be rewritten as:

$$y(x) = \frac{1}{24EI}\left[2wLx^3 - wL^2 - wx^4\right]. \quad (13)$$

Simplifying:

$$y(x) = -\frac{wx^2}{24EI}(L-x)^2 \quad (14)$$

3.2 Dynamic Response

To determine the dynamic characteristics of the beam, consider an elemental length of a beam dx, and the forces acting on it. (Figure 20)

Using Newton's second law in the transverse (y) direction:

$$\Sigma F_y = ma_y : V - V - \frac{\partial V}{\partial x}dx = \gamma dx\frac{\partial^2 y}{\partial t^2} \quad (15)$$

where γ = mass per unit length

Recalling from Euler-Bernoulli beam theory, for a beam of constant cross section:

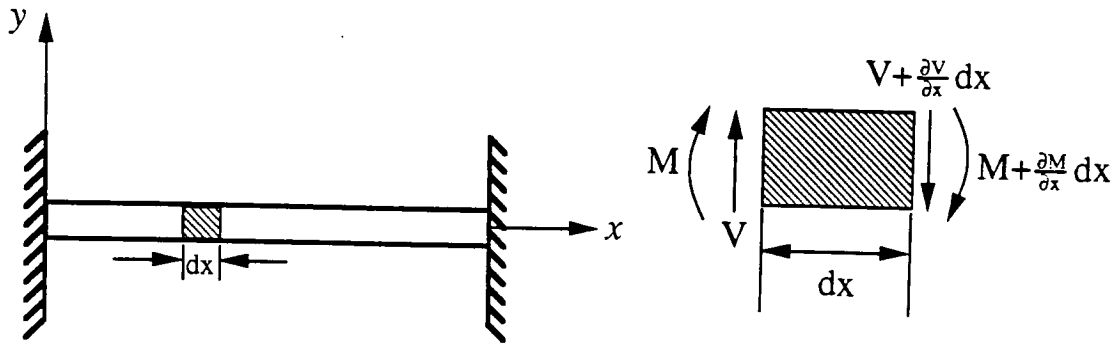

Figure 20: Elemental length of a beam

$$\frac{\partial V}{\partial x} = EI\frac{\partial^4 y}{\partial x^4} \tag{16}$$

Combining equations 15 and 16 we obtain

$$a^2\frac{\partial^4 y}{\partial x^4} + \frac{\partial^2 y}{\partial t^2} = 0 \tag{17}$$

where $a^2 = EI/\gamma$.

Using separation of variables to obtain a solution of the form $y(x,t) = o(x)q(t)$ yields:

$$\frac{\partial^4 y}{\partial x^4} = \frac{d^4\phi}{dx^4}q$$

and

$$\frac{\partial^2 y}{\partial t^2} = \phi\frac{d^2 q}{dt^2} = \phi\ddot{q}$$

Substituting these into equation 17 yields:

$$a^2\frac{d^4\phi}{dx^4}\frac{1}{\phi} = -\frac{\ddot{q}}{q} \tag{18}$$

Each side of equation 18 is an expression in ϕ or q only, so both sides must be equal to some constant (ω^2). Writing each of these sides equal to ω^2 yields:

$$\ddot{q} + \omega^2 q = 0 \tag{19}$$

and

$$\frac{d^4\phi}{dx^4} - (\frac{\omega}{a})^2\phi = 0 \tag{20}$$

The solution to equation 19 can be determined by inspection

$$q(t) = A\cos(\omega t) + B\sin(\omega t).$$

To solve equation 20 an exponential solution is assumed

$$\phi(x) = e^{rx}.$$

Taking the appropriate derivatives and substituting back into equation 20

$$(r^4 - k^4)e^{rx} = 0 \tag{21}$$

where $k^4 = (\omega/a)^2$.

Solving equation 21 yields the characteristic equation and its roots

$$r^4 - k^4 = 0$$

$$r_{1,2} = \pm k \text{ and } r_{3,4} = \pm \jmath k$$

Summing these solutions yields

$$\phi(x) = Ce^{kx} + De^{-kx} + Ee^{\jmath kx} + Fe^{-\jmath kx}. \tag{22}$$

Using identities and assuming that E and F are complex constants having the form of

$$E = C_3 - \jmath C_4 \text{ and } F = C_3 - \jmath C_4$$

equation 22 can be rewritten as:

$$\phi(x) = C_1\cosh(kx) + C_2\sinh(kx) + C_3\cos(kx) + C_4\sin(kx). \tag{23}$$

With solutions to both $\phi(x)$ and $q(t)$ obtained, the solution to equation 17 can be written as

$$y(x,t) = [C_1\cosh(kx) + C_2\sinh(kx) + C_3\cos(kx) + C_4\sin(kx)] * [A\cos(\omega t) + B\sin(\omega t)]. \quad (24)$$

To solve for the constants C_1, C_2, C_3 and C_4, the boundary conditions for the ends of the beam must be used. Hence,

$$y(0,t) = 0 \Rightarrow C_1 + C_3 = 0 \Rightarrow C_1 = -C_3 \quad (25)$$

$$y'(0,t) = 0 \Rightarrow C_2 + C_4 = 0 \Rightarrow C_2 = -C_4 \quad (26)$$

$$y(L,t) = 0 \Rightarrow C_1(\cosh(kL) - \cos(kL)) + C_2(\sinh(kL) - \sin(kL)) = 0 \quad (27)$$

$$y'(0,t) = 0 \Rightarrow C_1(\sinh(kL) + \sin(kL)) + C_2(\cosh(kL) - \cos(kL)) = 0 \quad (28)$$

to obtain a non-trivial solution to equations 27 and 28, we can solve for them in a matrix format

$$\begin{bmatrix} \cosh(kL) - \cos(kL) & \sinh(kL) - \sin(kL) \\ \sinh(kL) + \sin(kL) & \cosh(kL) - \cos(kL) \end{bmatrix} \begin{bmatrix} C_1 \\ C_2 \end{bmatrix} = \begin{bmatrix} 0 \\ 0 \end{bmatrix}$$

Taking the determinant of the 2x2 matrix and setting it equal to zero yields the characteristic equation

$$[\cosh(kL) - \cos(kL)]^2 - \sinh(kL)^2 + \sin(kL)^2 = 0 \quad (29)$$

Solving for the first ten values of Equation 29 yields Table 2. These are the first ten eigenvalues of the characteristic equation. It must be noted that there are an infinite number of eigenvalues of this equation.

The constants C_1 and C_2 cannot be solved for explicitly, so setting $C_1 = 1$ and solving equation 27 for C_2 yields

$$C_2 = \frac{\cosh(k_iL) - \cos(k_iL)}{\sinh(k_iL) - \sin(k_iL)} = \alpha_i$$

back substitution of C_1 and C_2 into equation 23 gives

$k_1 L$	=	4.73004074
$k_2 L$	=	7.85320462
$k_3 L$	=	10.99560784
$k_4 L$	=	14.13716549
$k_5 L$	=	20.42035225
$k_6 L$	=	23.56194490
$k_7 L$	=	26.70353756
$k_8 L$	=	29.84513021
$k_9 L$	=	32.98672286
$k_{10} L$	=	36.12831552

Table 2: Eigenvalues of the characteristic equation

$$\phi_i(x) = \cosh(k_i x) - \cos(k_i x) - \alpha_i[\sinh(k_i x) - \sin(k_i x)] \tag{30}$$

which is the modal shape function for a clamped-clamped beam.

The natural frequencies of a beam can be determined using the k_i's, the beam length L, and noting from equation 21 that $k_i^4 = (\omega_{n_i}/a)^2$. Hence

$$\omega_{n_i} = k_i^2 \sqrt{\frac{EI}{\gamma}}$$

where a has been replaced by EI (the equivalent stiffness of the system) and γ (the equivalent mass) as noted below Equation 17.

Warburton[16] specifies the equations of motion for a beam subjected to some force $f(t)P(x)$ as

$$\ddot{q}_i + c\omega_{n_i}\dot{q}_i + \omega_{n_i}^2 q_i = \frac{f(t)\int_0^L P(x)\phi_i(x)dx}{\int_0^L \rho(x)A[\phi_i(x)]^2 dx} \tag{31}$$

where subscript i represents the ith equation with the natural frequency ω_{n_i} and corresponding shape function ϕ_i, c is the damping coefficient, the denominator of the right hand side of the equation is the mass of the system, and i can range from 1 to ∞.

Given a beam of constant density and cross-section, and assuming that the input $f(t)P(x)$ takes the form $P\sin(\omega t)$ where ω is the forcing frequency, the right hand side of equation 31 reduces to

$$\frac{P\sin(\omega t)\int_0^L \phi_i(x)dx}{\rho AL}$$

The steady state response of equation 31 is [16]

$$q(t) = \sum_{i=1}^{\infty}\left[\frac{[P\int_0^L \phi_i(x)dx]\sin(\omega t - \varphi_i)}{\rho AL\sqrt{(\omega_{n_i}^2 - \omega^2)^2 + (c\omega_{n_i}^2\omega)^2}}\right] \tag{32}$$

where $\varphi_i = c\omega_{n_i}^2/(\omega_{n_i}^2 - \omega^2)$ represents the phase lag of the beam response to the input signal.

The deflection of the beam, $y(x,t)$, is calculated upon recalling the assumed form

$$y(x,t) = \phi(x)q(t) \tag{33}$$

as noted on page 23. Here $\phi(x)$ is the sum of all $\phi_i(x)$ as defined in Equation 30, and $q(t)$ is given by Equation 32.

If we assume no damping ($c = 0$) equation 33 can be expressed as

$$y(x,t) = \sum_{i=1}^{\infty}\left[\frac{[P\int_0^L \phi_i(x)dx]\phi_i(x)\sin(\omega t)}{\rho AL(\omega_{n_i}^2 - \omega^2)}\right] \tag{34}$$

For the extreme case when $\sin(\omega t) = 1$ the maximum deflected curve is

$$y_{max}(x) = \sum_{i=1}^{\infty}\left[\frac{[P\int_0^L \phi_i(x)dx]\phi_i(x)}{\rho AL(\omega_{n_i}^2 - \omega^2)}\right] \tag{35}$$

In this investigation a numerical solution of Equation 35 was conducted for $i = 1...10$ (i.e., ten harmonics of the dynamic solution).

3.3 Electrical Design Considerations

The capacitance,C, of a flat plate capacitor can be expressed as

$$C = \frac{\epsilon_0 A}{d} \tag{36}$$

Where $\epsilon_0 = 8.85\text{x}10^{-12}\frac{Farads}{meter}$, $A = wL$ (the area of the plate) and d = distance between the two plates.

In Equation 36, it is assumed that d is a constant dimension not varying along the length of the plate. For the current application, the dimension d will change in the x direction due to the transverse deflection of the beam. This will result in a modification of equation 36 of the form

$$C = \int_0^L \frac{\epsilon_0 w \, dx}{h - y(x)} \tag{37}$$

where h is the undeflected distance between the two plates, $y(x) = y_{static}(x) + y_{dyn}(x)$ where $y_{static}(x)$ and $y_{dyn}(x)$ are shown in Equations 14 and 35 respectively and w is the width of the cross-section. Using Equation 37 allows the capacitance to be calculated for both static and dynamic deflection cases.

4 Design and Fabrication

4.1 Design Considerations

The design of the microphone was governed by several constraints. Electrically, the microphone had to have a no-load capacitance of at least 10pF ($C_o \geq 10pF$) with a change in C_o of at least 10% when exposed to a 60dB sound field. This would allow the capacitance change to be measured with equipment available in the microelectronics laboratory. A manufacturing constraint required that the gap between the two plates be greater than 80 times the span over which that gap is maintained, measured from the non-clamped sides of the upper plate. This was necessary so that the sacrificial support material can be completely etched away between the two plates. Mechanically the microphone had to avoid resonance between 500–8000Hz, and have a membrane compliance such that the microphone would deform enough to have a measurable capacitance change under a typical 60dB sound pressure load. However, the microphone had to be rigid enough so that the top plate would not touch the bottom plate for that same load.

A design optimization problem was posed for reducing the microphone plate area in which a geometry (Figure 21), and the aforementioned design constraints were written. Mathematically we have

$$\text{Min OBJ}(L.w.h,t) = Lw \Leftarrow \text{plate area}$$

subject to the constraints:

$$\begin{aligned} G(1) &: C_o > 10\text{pF} \\ G(2) &: C_{dyn} > 1.10C_o \\ G(3) &: 80h > w \\ G(4) &: \omega_n > 10000\text{Hz}^1 \\ G(5) &: \delta_{dyn} < h \end{aligned}$$

[1]Placing ω_n well above the desired response range should provide a relatively flat response profile assuming little damping.

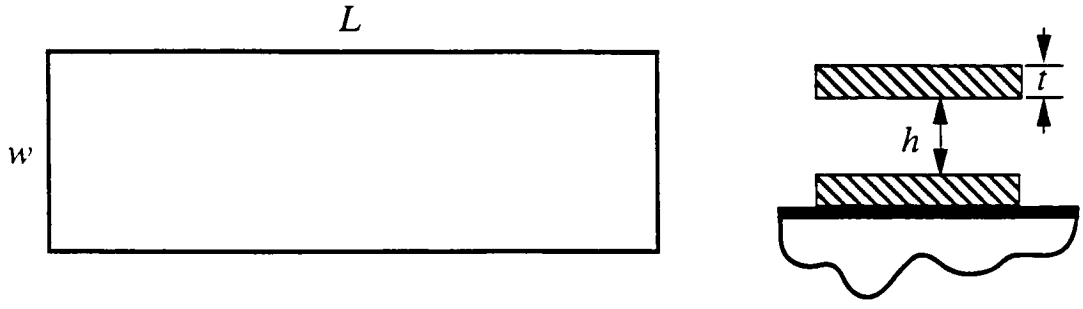

Figure 21: Microphone Geometry Conventions

where $G(1)$ governs the minimum no load capacitance, $G(2)$ defines the dynamic capacitance, $G(3)$ is the aspect ratio constraint as governed by manufacturing requirements, $G(4)$ assures no resonances below 10000Hz and $G(5)$ guarantees that the beam will not short-out on the bottom contact under dynamic loading.

Unfortunately, these criteria and the available construction materials[2] yielded no acceptable design that would satisfy all constraints. To obtain the frequency response desired, the top plate had to be reasonably stiff. This resulted in very small deflections under loading which translated to a very small capacitance change. To allow the small deflection to result in the necessary capacitance change, the two plates had to be brought close together. This violated constraint $G(3)$, due to the plate area requirement specified by constraint $G(1)$.

These problems were solved with two changes to the initial design. First, the lower plate was reduced in size relative to the top plate. This provided greater sensitivity by only using the area of maximum deflection to effect a capacitance change. This reduced the total capacitance of the microphone, but allowed constraints $G(2)$ and $G(3)$ to be met. To satisfy constraint $G(1)$, several smaller microphone elements were

[2]Polysilicon, E=150GPa, ρ=2300 kg/m^3. These are approximate values as found in [6] and [13]. The exact values of the material properties depend upon deposition type and deposition recipe.

ganged together in parallel to act as one sensing element. Enough of these elements could be connected to provide the necessary C_o. A new design was formulated from the revised set of constraints (Figure 22) where the optimization problem is posed as a minimization of upper plate area.

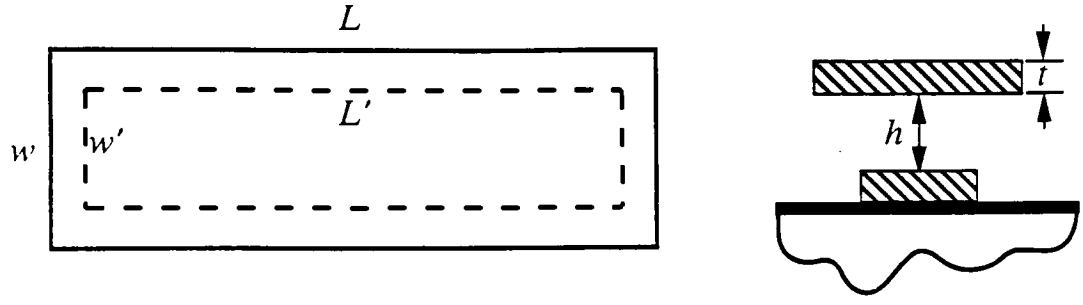

Figure 22: Microphone Geometry Conventions

$$\text{Min OBJ}(L, w, h, t, n) = Lw \Leftarrow \text{plate area}$$

subject to new constraints:

$$\begin{aligned} G(1) &: C_o > 10\text{pF} \\ G(2) &: C_{dyn} > 1.10C_o \\ G(3) &: 80h > w' \\ G(4) &: \omega_n > 10000\text{Hz} \\ G(5) &: \delta_{dyn} < h \end{aligned}$$

Here w' and L' (lower plate dimensions) are expressed as percentages of w and L (Y%, X% respectively) and n is the number of elements required to meet constraint $G(1)$. These constraints resulted in the design shown in Table 3.

For the design obtained, the frequency response and sensitivity curves were calculated (Figures 23, 24). The response curve is measured in decibels referenced to

ω_n	=	11138Hz	w	=	$40\mu m$
δ_d	=	$4.66\text{x}10^{-3}\mu m$	h	=	$0.05\mu m$
C_o	=	0.142pF	t	=	$0.5\mu m$
C_{dyn}	=	0.161pF	X%	=	32
w'/h	=	80	Y%	=	10
L	=	$600\mu m$	n	=	71

Table 3: Optimized Microphone Design

the static capacitance. The high frequency region of the curve depicted in Figure 23 indicates resonance, causing a greater change in capacitance for a given load. The sensitivity curve illustrates the static capacitance of the microphone with varying pressure. The sharp uprising at the high end of the pressure scale is caused by the plates almost coming in contact with each other and shorting out.

An initial prototype was made with many more sensing elements than required by the optimal design. This was done to provide a greater change in capacitance for a given signal, allowing amplification of the signal to be done externally from the microphone under test. Figure 26 depicts 140 of the individual sensing elements which were connected in parallel to yield a microphone array with a C_0 of 20pF. The single cell (Figure 25) is composed of a bottom plate, the sensing beam. and the two anchors. The array is formed by linking the top plates, and the bottom plates together in parallel.

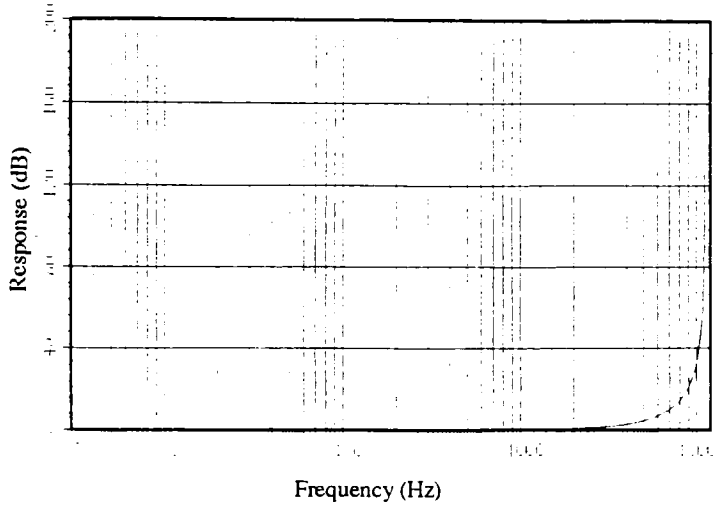

Figure 23: Calculated Response Curve for the Air-bridge Microphone

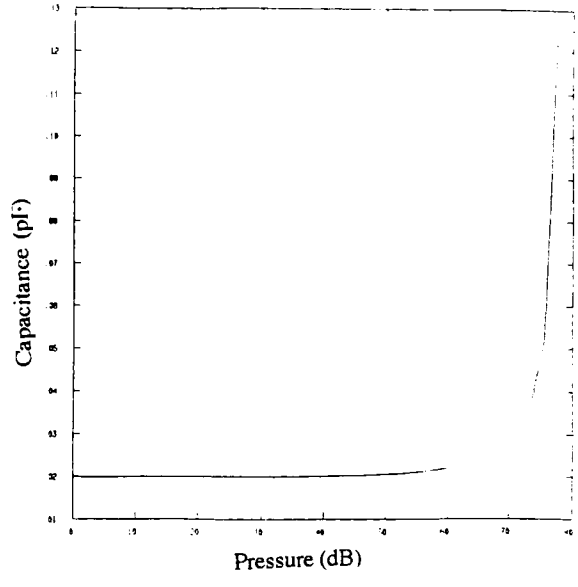

Figure 24: Calculated Sensitivity Curve for the Air-bridge Microphone

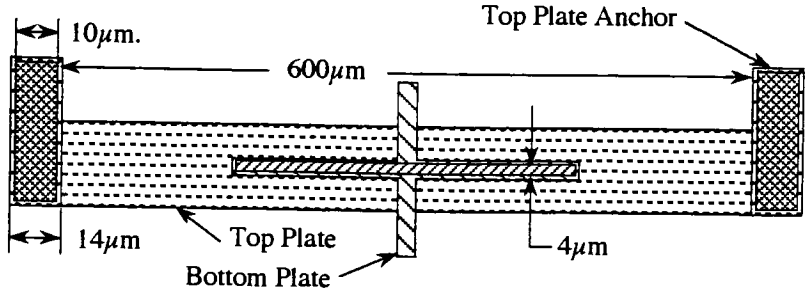

Figure 25: One Sensing Element for the Air-bridge Microphone (Top View)

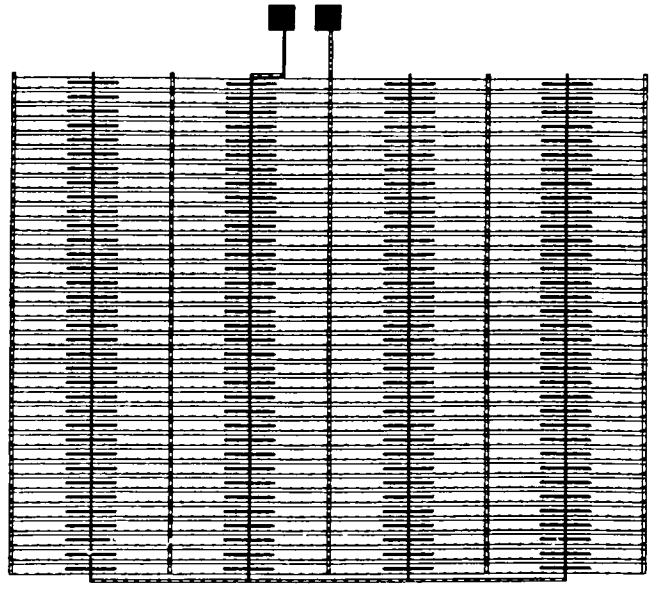

Figure 26: Air-bridge Microphone Array (Top View)

4.2 Microelectronic Construction

Construction of a three dimensional design such as a microphone is accomplished by a series of processes which include various depositions, and then selected etches. The basics of the deposit-etch process are illustrated in Figure 27

1. A bare surface is started with.
2. The material to be used in then deposited over the entire surface.
3. A photoresist is applied.
4. The photo resist is exposed using a mask.
5. The unwanted deposited material is etched away.
6. The photoresist is removed leaving the deposited material in the desired pattern on the surface.

To construct this microphone the following steps were used. Most all of these steps involve the use of the general procedure illustrated in Figure 27.

- The process is initiated on a bare silicon wafer of any orientation (Figure 28.a).
- A layer of silicon dioxide is grown in a furnace (Figure 28.b), then silicon nitride is deposited using low pressure chemical vapor deposition (LPCVD) (Figure 28.c). The Si_3N_4 and SiO_2 layers insulate the microphone from parasitic capacitances.
- The bottom plate of the microphone is made out of polysilicon deposited using LPCVD. It is then doped in a furnace with phosphorus to make the silicon conductive (Figure 28.d).
- Part of the sacrificial layer is formed using a spin-on-glass. Openings are etched in it for the spacer that will govern the distance between the top and bottom plates, and the top plate anchor (Figure 28.e).

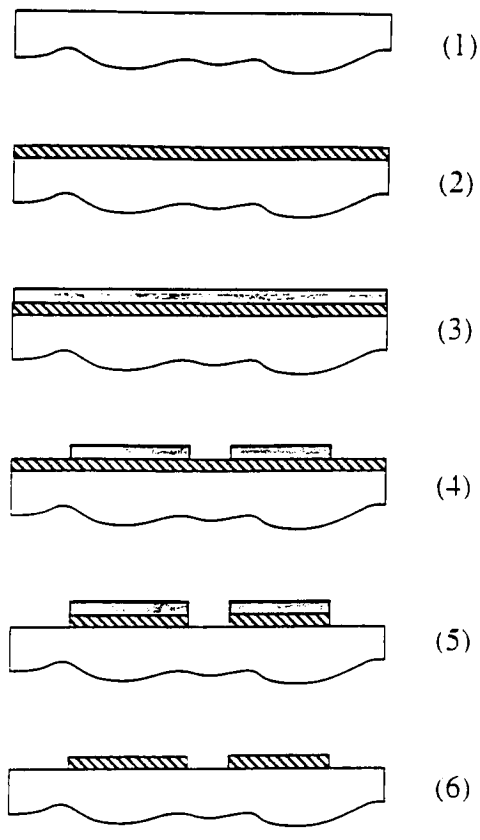

Figure 27: Steps used to construct a geometry on a wafer

- A silicon dioxide layer is grown to form a controlled spacer that will govern the plate separation (Figure 28.f). Silicon dioxide is used to control the between-the-plate spacing because it can be deposited with much greater control of deposition thickness than spin on glass.

- The polysilicon top plate is then deposited using another LPCVD process. The top plate is also doped with phosphorus to make it conductive (Figure 28.g).

- In the final step the spin on glass and silicon dioxide spacer are etched away to free the top plate from the rest of the structure (Figure 28.h). The microphone is then complete.

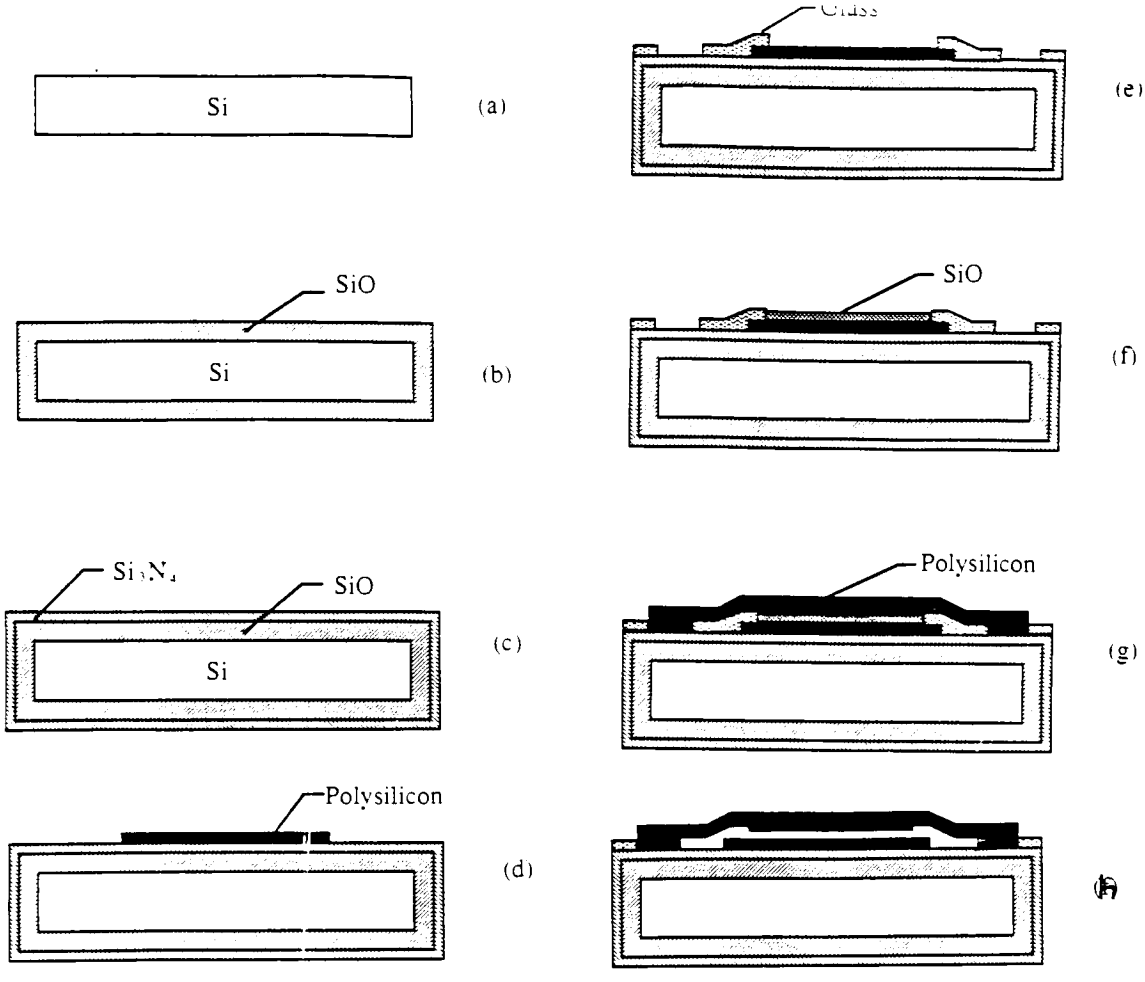

Figure 28: Processing steps for and Air-bridge Microphone

- Metal bonding pads are depositied to allow for electrical contact to be made with the microphone.

4.3 Documentation of Fabrication Process

The fabrication of the air-bridge microphone is detailed below.

Fabrication was started with four N-type 4 inch wafers. An RCA clean was performed prior to the first oxide growth.

Oxide was grown to a thickness of 9500Å in a wet-O_2 environment at 1100°C for 2.5 hours. Over top of the oxide, 1000Å of silicon nitride was grown at 810°C for 15

minutes. Without removing the wafers from the LPCVD, a 7000Å polysilicon layer was grown at 610°C for 70 minutes. The polysilicon was doped with a phosphorous spin-on dopant. The application was done at 3000RPM for 30 seconds. The dopant was driven into the polysilicon for 30 minutes at 1100°C in an N_2 environment. The doped glass was etched off in buffered hydrofluoric acid (HF) for 1 minute. The wafers were then coated with resist and patterned. After patterning, the polysilicon was etched using the reactive ion etcher (RIE). The etch was performed using 30sccm of SF_6, 10sccm of O_2, 100mTorr of pressure and 100W of power for 3.5 minutes. After etching, the photoresist was stripped with an oxygen plasma and the wafers RCA cleaned (Figure 29).

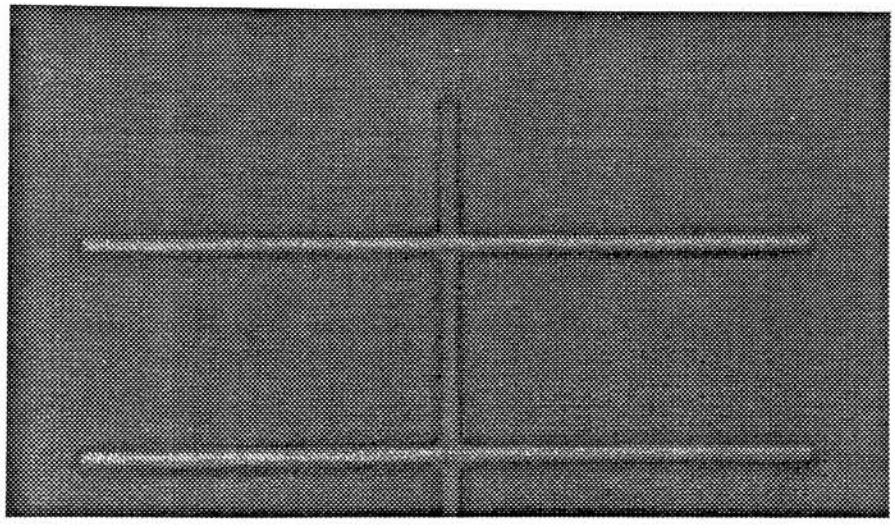

Figure 29: Bottom Polysilicon Plate

Spin-on-glass (4% P 4% B) was applied at 3000RPM for 30 seconds then pre-baked at 200°C for 15 minutes and baked at 1000°C for 30 minutes in an N_2 environment. The second patterning was done. to open holes for the oxide spacer and top plate anchor. After patterning, the glass was etched for 5 minutes in buffered HF. The photoresist was stripped and an RCA clean preformed (Figure 30).

The spacer oxide was grown in wet-O_2 at 900°C for 20 minutes. This grew a spacer 440Å thick (500Å target thickness). The third patterning step was performed

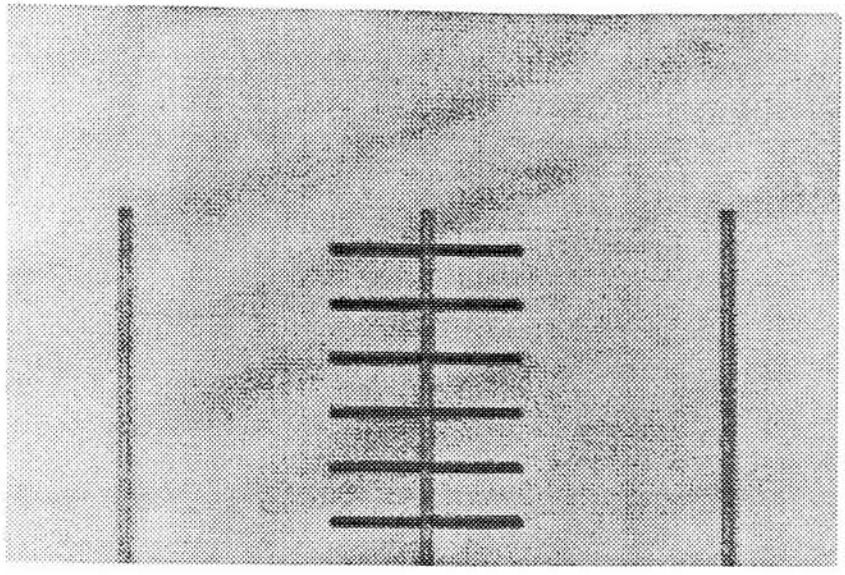

Figure 30: Oxide Openings Top plate Anchor

to open the top plate anchors. The SiO_2 was etched in buffered HF for 1.5 minutes. The wafers were then stripped and RCA cleaned (Figure 31).

The top plate polysilicon was grown at 610°C for 60 minutes to provide a 5000Å thick top plate. As with the bottom plate, phosphorus was used to dope the polysilicon. The fourth photo step was done, and the wafers etched in the RIE for 3 minutes using the same settings as before. The wafers were then stripped of photoresist (Figure 32).

The etch time required to remove all sacrificial material was unknown at the start of the sacrificial etch. A test wafer was etched for two hours in the HF solution, rinsed and then dried with an air gun. In Figure 33 it can be seen, from the color change, that half of the sacrificial material has been removed from underneath the top plate. Figure 34 shows the damage that was caused to another one of the microphones on the wafer by drying the wafer with an air gun. It is interesting to note that the remaining sacrificial material can be seen in the picture. After this first test etch, it was decided that the wafers would need at least an additional two hours in the HF etch to allow for complete removal of the sacrificial material. After rinsing in water, the wafers would be allowed to air dry to prevent damage caused by blow drying.

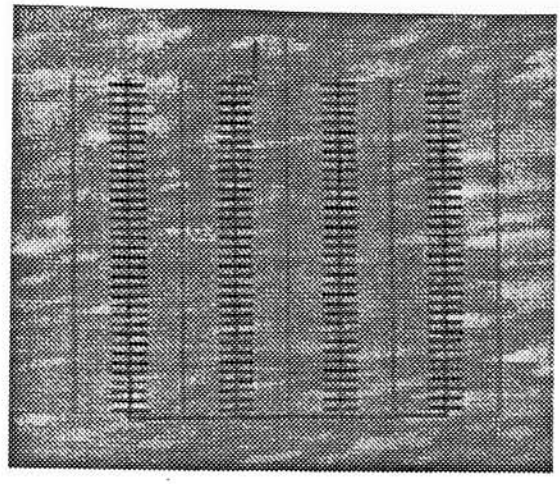

Figure 31: Top plate Anchor

After two more hours in the etch, several of the microphone arrays had been removed from the wafer surface. Upon submersion into the water rinse, the majority of the remaining microphones were washed away (see Results and Discussion for further comments on this topic). The wafers were rinsed for eight hours, removed from the rinse, allowed to air dry, and then examined.

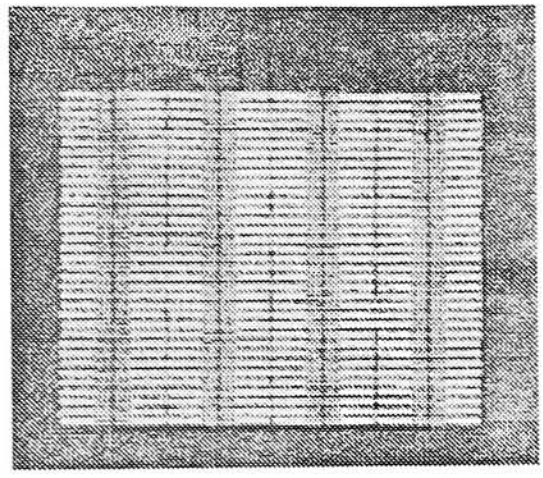

Figure 32: Top plate

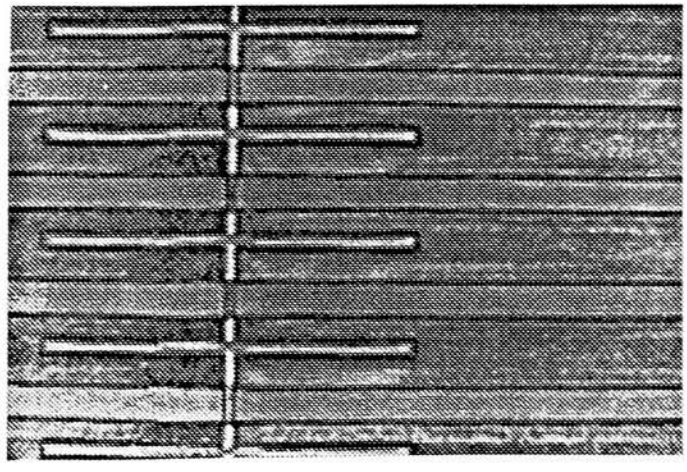

Figure 33: Structures after two hours in an HF etch

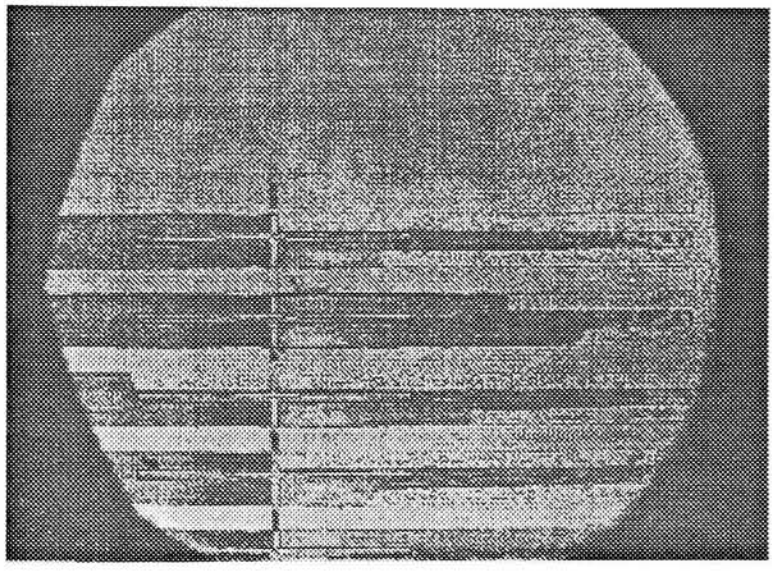

Figure 34: Damage caused by air gun drying

5 Results

5.1 Microphone Morphology via Light Microscopy

After four hours in the HF etch, Figure 35 depicts a typical part of one of the remaining air–bridge structures. The anchors have been undercut, allowing the top plates to float away. Figure 36 shows one of the completely released top plates under three attached top plates. This picture confirms that the sacrificial material has been completely etched away, leaving an air-gap between the top plate and the wafer surface. The wafers were sectioned, and the a scanning electron microscope (SEM) was used to allow a more detailed examination of the remaining air–bridge structures.

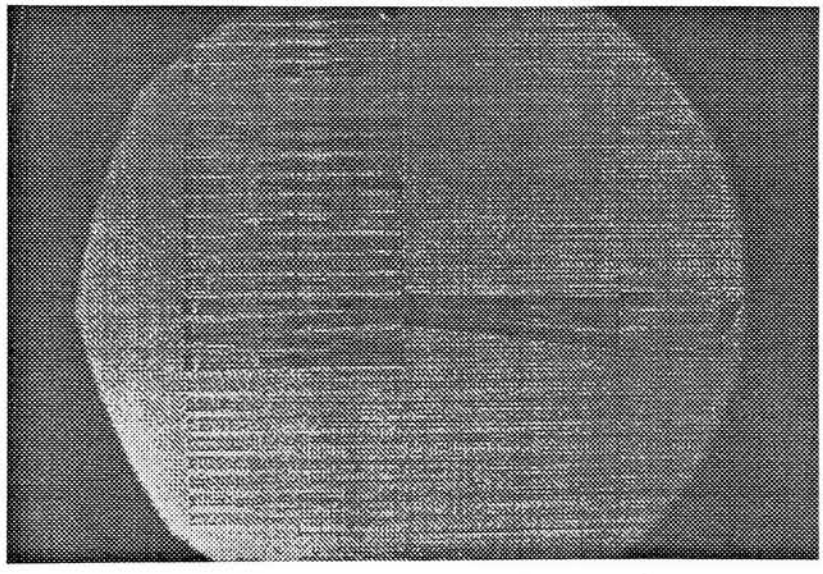

Figure 35: Top plates floating away due to under-cutting

5.2 Microphone Morphology via Scanning Electron Microscopy (SEM)

Examination of the wafers using the SEM provided many insights into errors in the design and processing of the microphones. Microphone sections were examined from both two and four hour etch tests to gather as much information as possible to aid

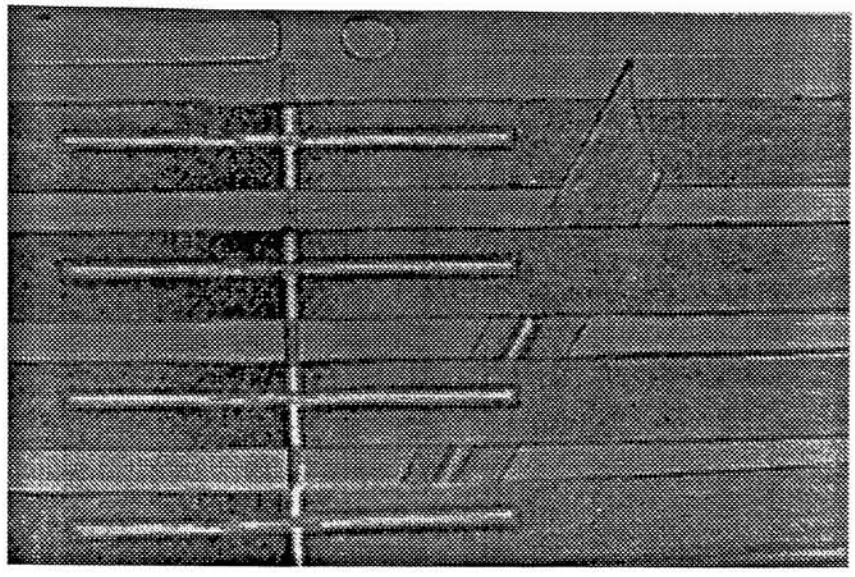

Figure 36: Floating top plate under several secured top plates

in a redesign.

On inspection of the first wafer sample (Figure 37), it is noted that several of the bridges have bowed significantly. It can also be seen that the bottom plate has been lifted off of the wafer surface along with the top plate. A closer look at the bowed section (Figure 38) shows a particle of some sort lodged under two of the bowed top plates. Examining the anchors on the left side of these bowed structures (Figure 39) shows that they have separated from the wafer surface. There is pitting on the anchor strip, indicating the anchor openings were not etched sufficiently in a previous step. It is theorized that the anchors were released upon submersion into the water rinse, and a particle was trapped under the beams.

In Figure 40 the lower plate has been removed along with the top plate. The attachment of the two plates could have been caused in two ways. First, the sacrificial material might not have been completely etched away, leaving the two plates to still be bonded together. Second, there still might have been some water or HF in the gap between the two plates and due to the small gap, capillary forces held the plates together.

Figure 41 depicts a situation where one of the bottom plate traces has been freed

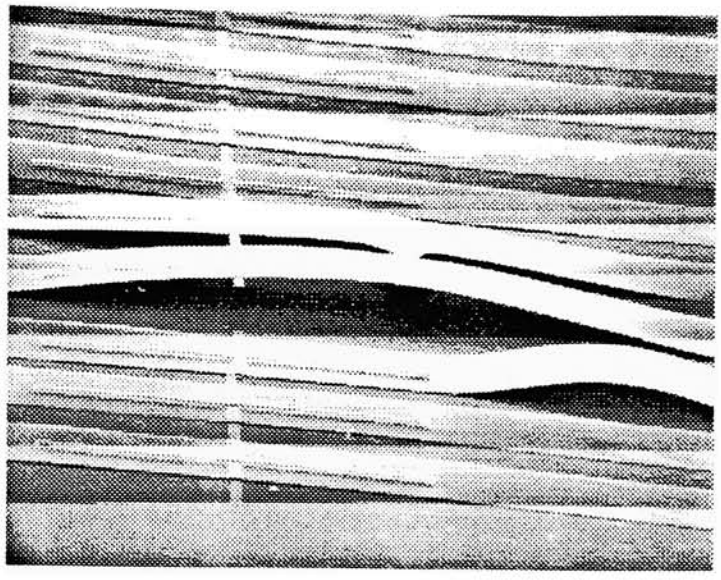

Figure 37: Bowing in top plate due to contamination

and has wedged itself under two top plates. Again, the pitting of the anchors can be seen on the right hand side of the photograph. Similar separation of the bottom plate traces is observable at other areas of the wafer as previously noted in Figure 39. Figure 42 depicts a wafer section after a two hour etch. Sacrificial material still remains to be etched, and the shattered top plates were likely damaged by blow drying. Turning the sample 90°clockwise and magnifying the top-bottom plate interface (Figure 43), it can be seen that the bottom plate has started to separate from the wafer surface. The remaining sacrificial material can also be seen on the exposed surface of the bottom plate as the pitted layer located near the bottom center of the picture.

The air-gap and bottom plate interface is shown under higher magnification (20,000X) in Figure 44. The top plate is suspended above the wafer surface, but closer inspection shows that the top plate has formed a hanging appendage that extends down to the wafer surface. This appendage would prevent the beam from vibrating, as well as interfere with the migration of etchant under the top plate.

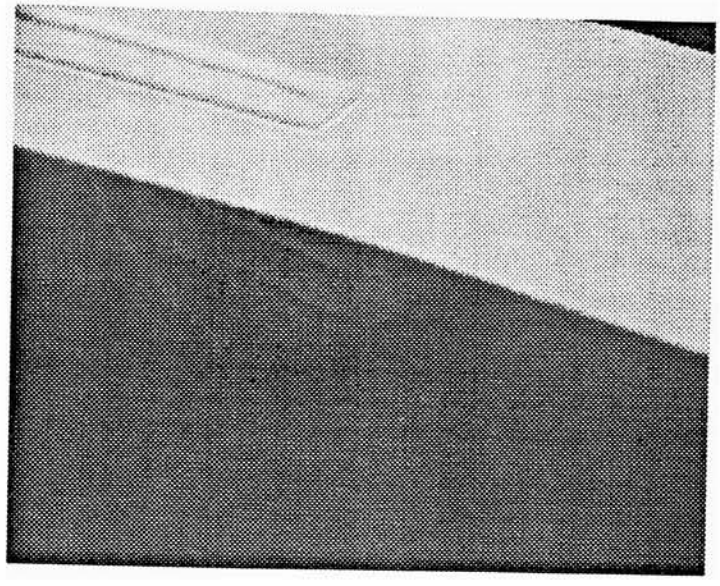

Figure 38: Dust particle causing the bowing of the top plate

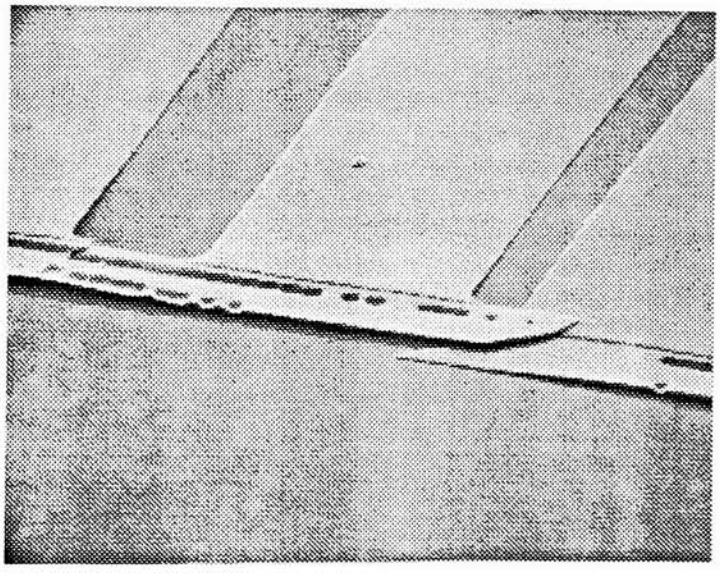

Figure 39: Fractured anchor bar on bowed plate

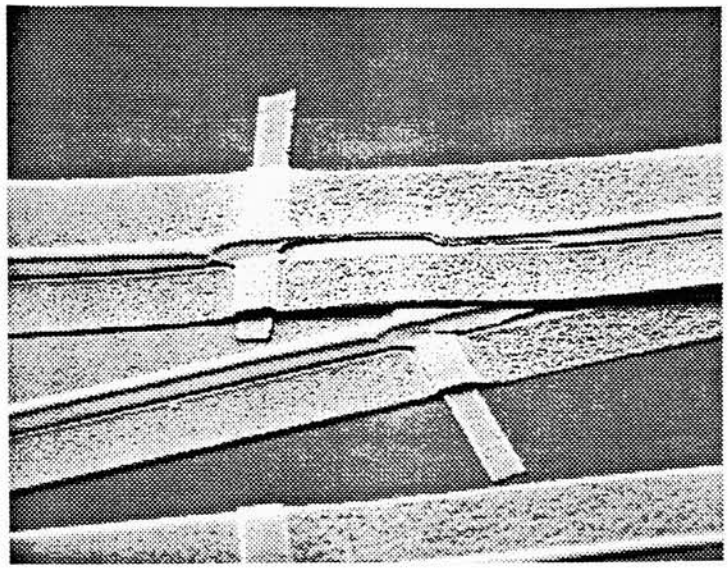

Figure 40: Top and bottom plates pulled off of the wafer surface

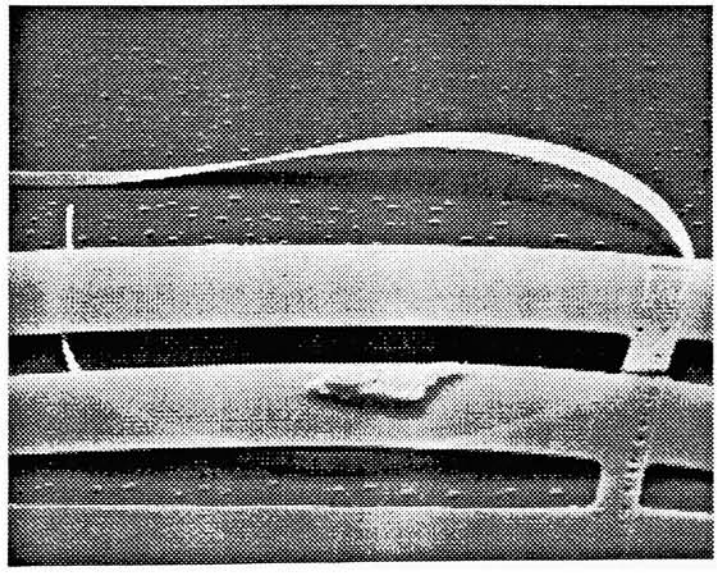

Figure 41: Lower trace wedged under top plates

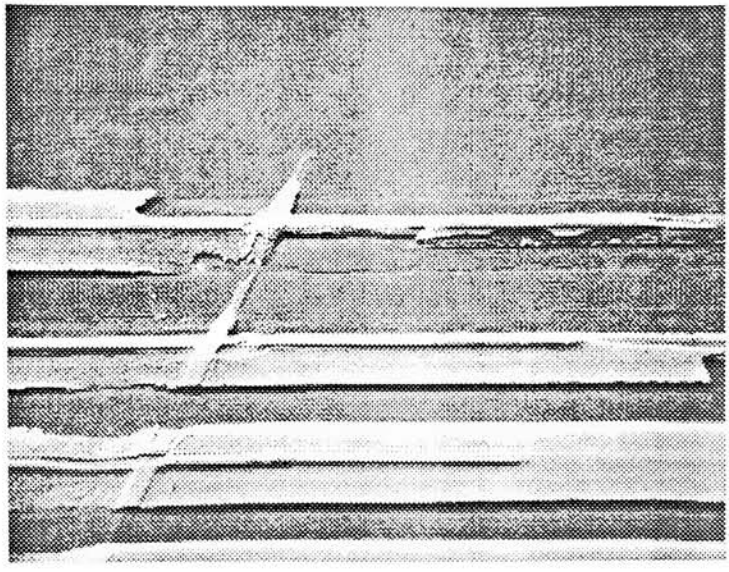

Figure 42: Damage caused to top plates by blow drying

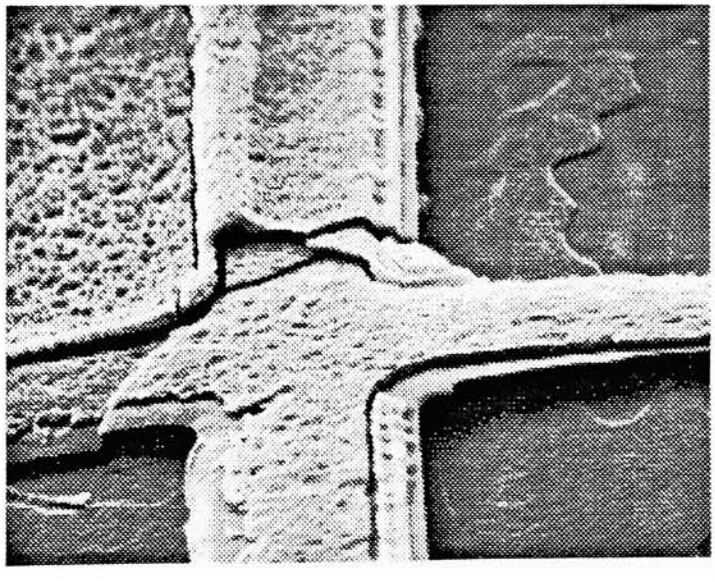

Figure 43: Magnified area of blow drying damage

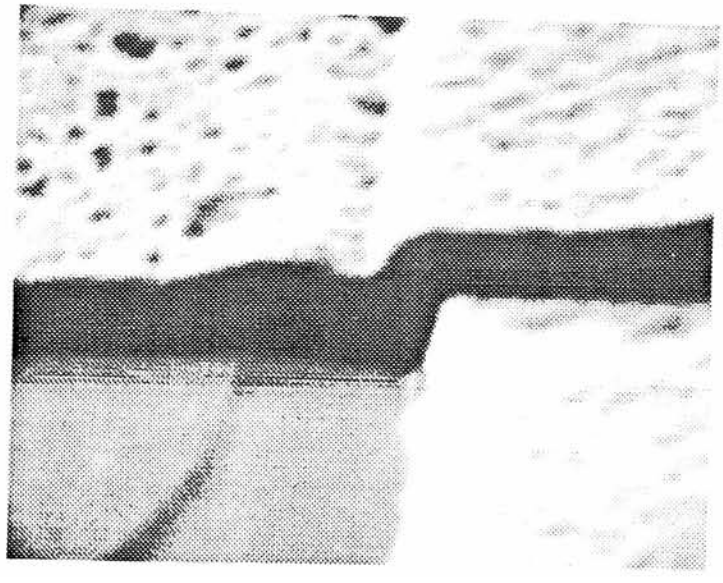

Figure 44: Close up of air-gap–top plate interface

6 Discussion of Results

Even though the microphones were not useable, much was learned from construction of the first prototypes.

The major flaw in the initial design was the failure to account for the HF undermining of the silicon nitride during the long sacrificial etch. Both the top and bottom plates were affected by this design flaw. Wider anchors should be incorporated in the re-design along with bottom plate traces at least as wide as the top plate. The new design should prevent the top plate anchors from being placed upon sacrificial material. To accomplish this, the anchor openings in the glass and oxide photo levels should be made larger than the anchor pad. This would help to prevent the anchors from being undercut. A possible design implementing these changes is shown in Figure 45.

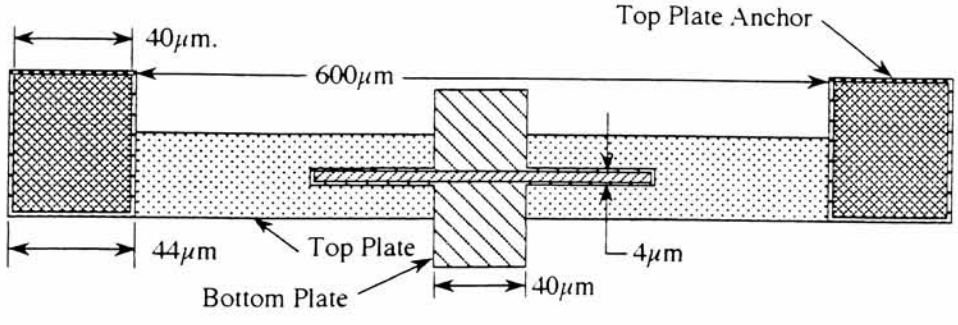

Figure 45: New proposed microphone design

After the sacrificial material has been etched from between the two plates, the microphones are fragile and susceptible to damage by subsequent processing. Hence, appropriate precautions and still-air drying should be employed after removal of the sacrificial material. In the current design, an additional metallization step is required after the sacrificial etch to place test probe pads onto the microphone traces. This

additional step could be eliminated by fabricating the bonding pads using polysilicon during the top plate polysilicon deposition. The sacrificial etch would then be the final processing step, preventing possible damage to the air–bridge microphones due to metal bonding pad deposition as required by the current design.

Scanning electron micrographs of the top plate-bottom trace interface (Figure 44) showed that an appendage hung down to the wafer surface which should be eliminated from the next design iteration. This appendage could have been caused by poor coverage of the spin-on-glass near existing geometries, or poor alignment of the spin-on-glass photomask. As a remedy, an oxide could be grown as a sacrificial material instead of the glass, and better alignment sought for this photomask.

The recipes for the depositions and etches were determined during the course of this thesis (Section 4.3), and have yielded acceptable results with the exception of the air-gap spacer. The air-gap is the critical dimension of this design. In the current prototype the gap was undersized by 60Å. The growth time for this spacer should be increased accordingly[3] for this step, erring on the side of increased dimension if it is not exact.

The implementation of the aforementioned design and fabrication changes should allow for the fabrication of a useable microphone. An acoustic testing regime has been established as detailed in Appendix A, and the necessary test fixtures constructed. It is hoped that these changes will be used to produce the next generation microphone that meets the design goals.

[3]The amount of time to add to this oxide growth should be determined via the wet-O_2 growth rate tables.

A Proposed Microphone Testing Strategy

To evaluate the success of the air-bridge microphone design, the air-bridge microphones needed to be tested against some reference. For this investigation the test reference proposed was a Bruel & Kjaer 4133 1/2" Microphone. The 4133 microphone is a "research" grade microphone with a frequency response ranging from 20Hz to 44kHz. Over this range it has a sensitivity of 12.6mV/Pa. Figure 46 shows the response curve and other relevant data pertaining to the 4133 microphone.

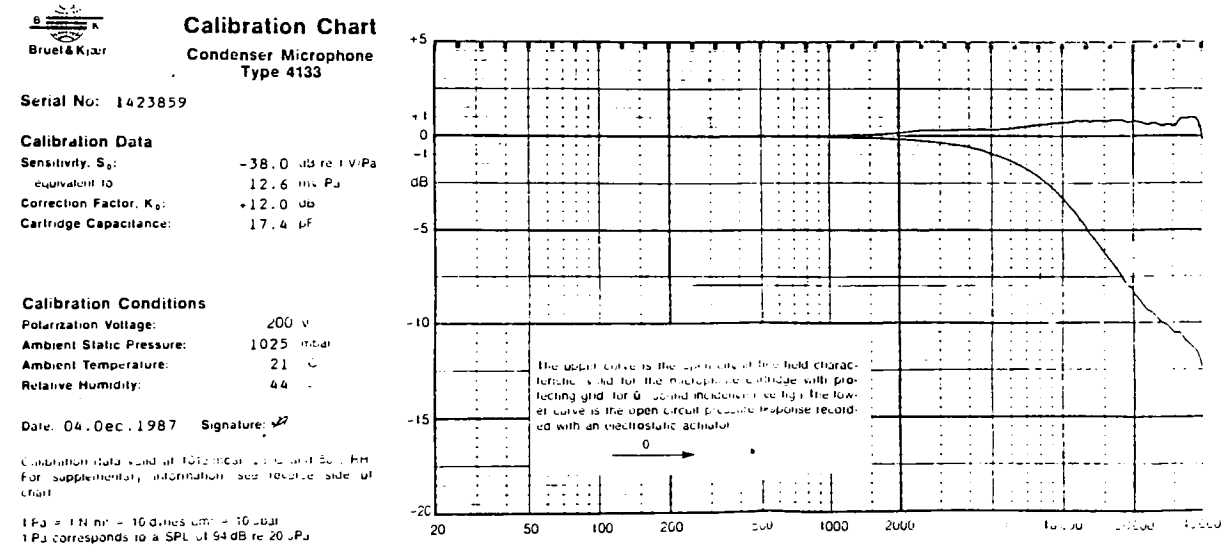

Figure 46: Response curve for B&K 4133 refrence microphone

The 4133 microphone is used in conjunction with a B&K 2607 Measuring amplifier to measure the intensity of a given sound field with great precision. To measure the output of the air-bridge microphone, the capacitance change has to be converted to a voltage change. Conversion of capacitance to voltage can be accomplished using a capacitance meter with its analog voltage output monitored on an oscilloscope. All testing should be done in a semi-anechoic chamber designed to allow the reference and air–bridge microphones to be exposed to free field sound, while being insulated from outside noise. Such a chamber has been designed and fabricated (Figure 47).

To evaluate the frequency response of the air-bridge microphone, both it and the 4133 microphone should be placed in the semi-anecohic chamber. and a pure tone

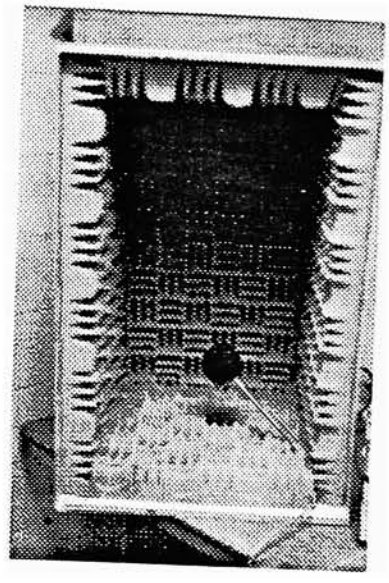

Figure 47: Experimental Test Set-up

sound introduced into the chamber via a function generator, preamplifier and acoustic speaker apparatus. The 4133 microphone would provide information on the intensity of the sound field for a known frequency. The air–bridge microphone's response would be measured using the capacitance meter. By varying the frequency of the pure tone, and keeping the intensity of each tone the same, a plot of frequency response could be made similiar to that in Figure 23.

To measure the sensitivity of the microphone, the same experimental set-up should be used, but instead of varying the frequency, the intensity of the tone should be changed to measure the change in air-bridge microphone output. This could be done over a range of frequencies in the air-bridge microphone design range (500-8000Hz). A plot of intensity (SPL) could then be constructed similiar to that previously depictied in Figure 24.

The two tests described above should completely characterize the microphone and allow suitable comparison to previously constructed microphones.

References

[1] AARON J., *An Economic Study of the United States Hearing Aid Industry: A Demand Side and Supply Side Examination*, The University of Illinois at Chicago, Ph.D. Thesis, 1987.

[2] VON BEKÉSY G., *Sensory Inhibition*, Princeton University Press, 1967.

[3] VAN BERGEIJK W. A., J. R. PIERCE AND E. E. DAVID, JR., *Waves and the Ear*, Anchor Books Doubleday & Company, Inc., 1960.

[4] BRUEL & KJAER INSTRUMENTS, INC., *Measuring Sound*, 1984.

[5] BERGQVIST J. AND F. RUDOLF, A New Condenser Microphone in Silicon, *Sensors and Actuators A*, Vol. 21, 1990, pp. 123–125.

[6] CHO, YOUNG–HO AND A. P. PISANO , Optimum Structural Design of Micromechanical Crab–leg Flexures with Microfabrication Constraints. *DSC-Vol 19, Microstructures, Sensors and Actuators*, American Soc. of Mechanical Engineers 1990, pp. 31–49.

[7] CLARK G. M., Y. C. TONG AND J. F. PATRICK, *Cochlear Prostheses*, Churchill Livingstone, 1990.

[8] FAY T. H., Implantable Auditory Systems. *The Vanderbilt Hearing-Aid Report II*, 1990. Ch. 9, pp. 101–119.

[9] ed.R. F. GRAY, *Cochlear Implants*, College-Hill Press, Inc., 1985.

[10] HOLM D. AND G. HESS, A Subminiature Condenser Microphone with Silicon Nitride Membrane and Silicon Back Plate. *J. Acoust. Soc. Am.*, Vol. 85, January 1989, pp. 331–336.

[11] JAMES M. L., G. M. SMITH, J. C. WOLFORD AND P. W. WHALEY. *Vibration of Mechanical and Structural Systems*. Harper & Row, Publishers, 1989.

[12] KUHNEL W., Silicon Condenser Microphone with Intergrated Field-effect Transistor, *Sensors and Actuators A*, Vol. 25, 1991, pp. 521–525.

[13] PETERSEN, K. E., Silicon as a Mechanical Material, *Proceedings of the IEEE*, Vol. 70, No. 5, May 1983, pp. 420–433.

[14] SESSLER G. M., Acoustic Sensors, *Sensors and Actuators A*, Vol. 25, 1991, pp. 323–330.

[15] SHIGLEY, J. E. AND L. D. MITCHELL, *Mechanical Engineering Design.* McGraw-Hill Book Company ,1983, p.881.

[16] WARBURTON G. B., *The Dynamical Behaviour of Structures*, Pergamor Press 1976, pp.139–151.

[17] WEISE, K. D., Micromechanical Sensors, Actuators and Systems, *DSC-Vol 32, Micromechanical Sensors, Actuators, and Systems*, American Soc. of Mechanical Engineers 1991, pp. 1–14.

[18] VOORTHUYZEN J. A., A. J. SPRENKELS, A. G. H. VAN DER DONK, P. R. SCHEEPER AND P. BERGVELD, Optimization of Capacitive Microphone and Pressure Sensor Performance by Capacitor-electrode Shaping, *Sensors and Actuators A*, Vol. 25, 1991, pp. 331–336.